STRUCTURAL BIOLOGY

Mechanistic insights into 50*S* precursor recognition and targeting by erythromycin resistance methyltransferase

Sombuddha Sengupta[1]†, Rajat Mukherjee[1]†, Michael Pilsl[2], Siddharam Bagale[1], Arijit Das Adhikary[1], Aditi N. Borkar[3,4], Pushpangadan Indira Pradeepkumar[1], Christoph Engel[2], Arindam Chowdhury[1], Prem S. Kaushal[5], Ruchi Anand[1]*

Erythromycin resistance methyltransferases (Erms) confer resistance to macrolide, lincosamide, and streptogramin B antibiotics by methylating an internal base (A2058, *E. coli* numbering) in an elusive precursor ribosomal state. Here, we capture the 50*S* ribosomal precursor–Erm complex by cryo-EM and show that a transient pocket formed in the early steps of ribosome biogenesis, situated 35 angstrom from the methylation site, serves as an anchor for the auxiliary C-terminal domain of Erm, thereby playing a crucial role in achieving specificity in this short-lived substrate with evolving structural features. Cryo-EM reveals that the catalytic Rossman fold of Erm undergoes a swaying motion to facilitate substrate scouting. Corroboratory smFRET studies show that for effective catalysis, Erm transitions between multiple conformations, an effective strategy adopted to orient the dynamic helix where methylation occurs. Unraveling this unique mechanism of targeting adopted by Erm paves the way for selective design of allosteric inhibitors directed toward reversing MLS_B resistance.

INTRODUCTION

Antibiotic resistance is a silent pandemic spreading rapidly at an alarming pace and is projected to cause more than 10 million deaths annually by the year 2050 if effective therapies to combat it are not pursued (*1*, *2*). Drug resistance partly originates from bacteria such as *Streptomyces*, which produce numerous antibiotics while harboring sophisticated resistance mechanisms to protect themselves against these molecules (*3*). Because of rampant antibiotic misuse, several pathogenic organisms have borrowed resistance cassettes via horizontal gene transfer from these progenitors, with target modification being a notably effective route to neutralize the effect of drugs (*4*). The ribosome is a primary target for several antibiotics, which act by binding to functionally critical sites halting protein synthesis (*5*). Resistance to ribosome targeting antibiotics manifests in several ways, with posttranscriptional modification of the ribosomal RNA (rRNA) being one of the leading mechanisms (*6*). For instance, resistance to macrolide, lincosamide, and streptogramin B (MLS_B) class of antibiotics, which bind near the nascent peptide exit tunnel (NPET) of the 50*S* ribosomal subunit, occurs via methylation of the N6 position of the unique adenine base, A2058 (*Escherichia coli* nomenclature), in the 23*S* rRNA (*7*). These drug molecules interact with the nucleotides that line the NPET, thereby obstructing the growing peptide chain in bacterial ribosomes (*8*). Consequently, the MLS_B family of antibiotics has proven to be greatly effective in treating a wide range of bacterial infections.

The macrolide family of antibiotics composes a 12- to 16-member macrolactone ring containing compounds functionalized with rare sugars such as cladinose and desosamine (*9*). Resistance toward this class of antibiotics, as mentioned earlier, arises primarily via posttranscriptional modifications that compromise the interactions of these drugs, especially the rare sugar moieties with ribosomal bases. This is primarily due to the action of select enzymes that are present exclusively in drug-resistant pathogenic strains. Erythromycin resistance methyltransferase (Erm) is an *S*-adenosine L-methionine (SAM)–dependent Rossmann fold harboring class of enzyme that mono- or dimethylates A2058 present in the NPET and thereby plays a key role in drug resistance (*10*). While monomethylation leads to moderate resistance, dimethylation has been reported to be associated with more aggressive resistant phenotypes (*11*). A recent high-resolution crystal structure of the Erm-methylated *Thermus thermophilus* 50*S* ribosomal subunit has shed light on the molecular mechanism of resistance via this route (*12*). The observations reveal that the methylation of the N6 atom of A2058 disrupts an existing water-mediated bridge between A2058 and the dimethyl-amino group of the desosamine sugar of the macrolide, which reduces drug affinity and dislodges it from the NPET of the ribosome.

Beyond its role as a resistance marker, rRNA methylation plays a crucial role in ribosomal biogenesis. The enzymes involved in ribosomal biogenesis are evolutionarily prehistoric, and it is possible that both resistance-conferring rRNA methyltransferases (MTases) as well as those involved in ribosomal biogenesis stem from a common evolutionary predecessor (*13*). Recent studies exploring the basis of substrate specificity and targeting in pathogenic Erms revealed a close paralogous connection to KsgA, an MTase that serves as a 30*S* biogenesis factor (*14*). Chimeric versions of KsgA that had unique loop elements swapped from Erm into the KsgA scaffold imparted KsgA the ability to modify RNA templates recognized by Erm. Bacterial cell lines harboring the chimeric KsgA variants also exhibited a gain of resistance when exposed to increasing concentrations of erythromycin. The ease with which pathogenic Erm and KsgA can switch substrate specificity is primarily due to the highly conserved catalytic core present in almost all N6 MTases (*15*). Previous studies have shown that this specific mechanism of methyl transfer is operational not only for RNA MTases such as TFB1M and DimI (homologs of KsgA) (*16*, *17*) but is also recurrent in DNA MTases such as

[1]Department of Chemistry, Indian Institute of Technology Bombay, Powai, Mumbai 400 076, Maharashtra, India. [2]Regensburg Centre for Biochemistry, Structural Biochemistry Group, University of Regensburg, D-93053 Regensburg, Germany. [3]One Virology, Wolfson Centre for Global Virus Research, University of Nottingham, Nottingham LE12 5RD, UK. [4]Faculty of Medicine and Health Sciences, School of Veterinary Medicine and Science, University of Nottingham, Nottingham LE12 5RD, UK. [5]Structural Biology and Translation Regulation Laboratory, UNESCO-DBT Regional Centre for Biotechnology, NCR Biotech Science Cluster, Faridabad 121 001, Haryana (Delhi NCR), India.
*Corresponding author. Email: ruchi@chem.iitb.ac.in
†These authors contributed equally to this work.

M•*Taq*I and Dam, a crystal structure of which has been solved with its cognate DNA substrate (*18*, *19*). These Rossmann fold–containing MTases operate via a ubiquitous mechanism with the active site comprising an aromatic residue that enables π-π interaction–mediated stabilization of the target nucleobase that in most cases has been shown to undergo an almost 180° flip positioning itself into the catalytic cavity. The cofactor SAM binds inside the extended active site pocket with its nucleobase stabilized by a β-turn created via a "XGXG" motif, and its ribose sugar is anchored via interaction with conserved acidic residues (E/D). The methyl transfer is mediated via a loop harboring a [D/N/S][I/L]P[Y/F] motif that both orients and mediates the transfer of the methyl group of SAM. This S_N2 mechanism (*20*) of methyl transfer (Fig. 1A) is facilitated via the formation of two hydrogen bonds between the nitrogen atom of the target base with D/N/S and the proline residues present in this region. Thus, a common catalytic motif governs methylation in the N6 targeting enzyme superfamily, however with select loop elements, unique to each MTase, which control its selectivity and targeting. The similarity in the mode of catalysis in this enzyme family reasserts the strong evolutionary link between ribosomal biogenesis factors and resistance-conferring MTases.

Despite having a universally conserved mechanism of methyl transfer and similar structural folds, the key question remains as to how an individual MTase identifies its target substrate with high precision. This question is particularly intriguing in the case of Erm, which functions during the early stages of ribosomal biogenesis and likely acts on transient assembly intermediates (*21*). The complexity of Erm targeting is even more convoluted as this enzyme has to identify its target site in a highly heterogeneous environment during the course of ribosomal assembly which itself proceeds via multiple parallel pathways with several ephemeral metastable states (*22*). Nevertheless, during the finely orchestrated process of ribosomal biogenesis, Erm successfully identifies a window and efficiently imparts the resistance mark. However, the exact stage during ribosomal assembly where Erm successfully docks and can access the N6 position of A2058 remains hitherto unknown (Fig. 1B). Through this work, we provide insights into the mechanism of Erm recognition and targeting by determining the cryo–electron microscopy (cryo-EM) structure of the functional complex of Erm with its cognate 50*S* ribosomal precursor state. Further, we use single-molecule fluorescence resonance energy transfer (smFRET) to underscore the intrinsic dynamic nature of the interaction of these enzymes with their ribosomal precursor. Delineating the detailed molecular mechanism of Erm-mediated resistance at the structural level has broader implications as it not only provides key insights into understanding substrate recognition of rRNA MTases acting on transitory ribosomal states but also serves as a step forward in the design of inhibitors that can impede the action of these resistance-conferring MTases.

RESULTS

Identifying the ribosomal substrate of Erm

Previous reports claimed that Erm shows no discernible methylation toward the mature 50*S* subunit (*21*), mostly because A2058 that lines the wall of the NPET is buried deep within the ribosome's mature state, rendering the base inaccessible. Thus, a precursor state of the ribosome, where domain V (in the 23*S* rRNA) is still unassembled, could be a likely substrate of Erm. This would ensure that A2058 is exposed, allowing Erm to methylate it. Thus, to capture 50*S* precursor states, we undertook a strategy proposed by Suzuki and

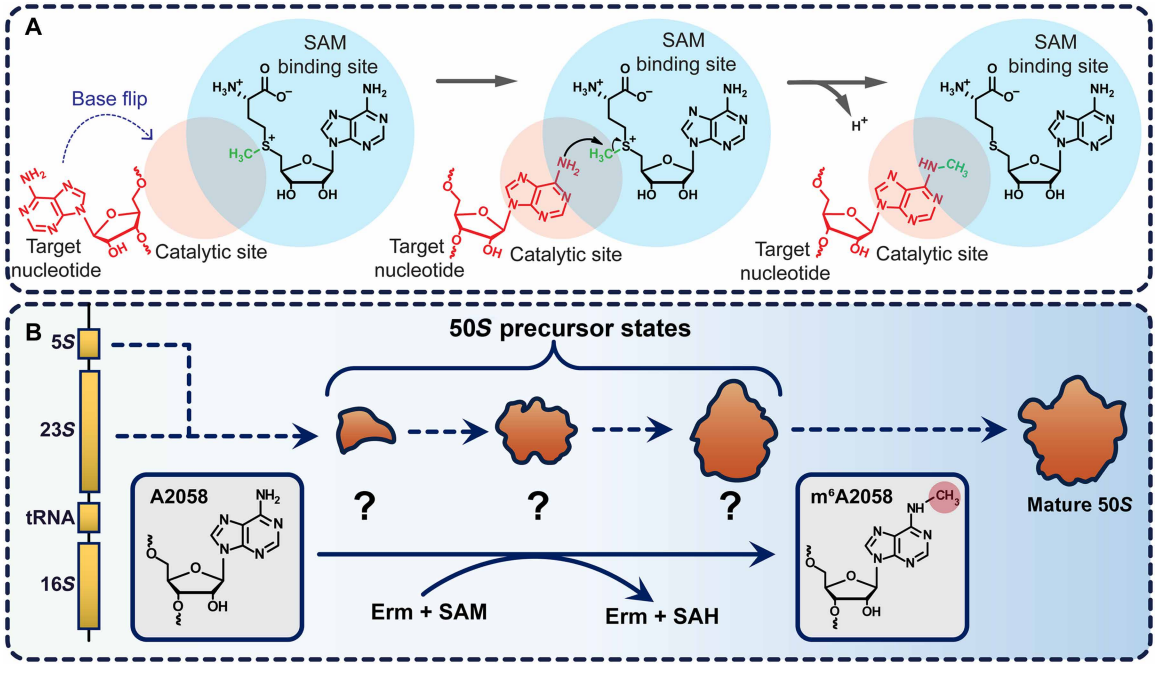

Fig. 1. Reaction mechanism and substrate specificity of Erms. (**A**) S_N2 mechanism of methyl transfer by N6 MTases where the target base flips into the catalytic site (shown as dashed arrow). The orange-colored zone denotes the catalytic site, while the blue zone denotes the cofactor, SAM binding site. The methyl group to be transferred has been shown in green. (**B**) Schematic depicting Erms targeting precursor states of the 50*S* ribosomal subunit. However, the actual ribosomal assembly state that serves as a substrate for Erms remains uncharacterized.

co-workers (*23*) that slows down ribosome biogenesis in vivo but does not halt the formation of the mature 50*S* particle. Here, the mutation U2552C (*E. coli* nomenclature) in helix 92 (H92; all helices in the 23*S* rRNA have been referred to as HXX from here on, where "XX" refers to the helix number; for helices in the 16*S* rRNA, hXX has been used) of domain V in the 23*S* rRNA prevents the 2′-*O*-methylation of the base by the biogenesis factor RlmE, effectively leading to the accumulation of ribosomal precursors (fig. S1). The ribosomal profile obtained from the U2552C strain revealed a distinct precursor peak that sedimented differentially from both the 30*S* and 50*S* subunits in the sucrose gradient (Fig. 2A). Fractions containing the precursor peak were isolated and subjected to in vitro methylation assay using tritium-labeled SAM with one of the extensively studied Erms, ErmC′. A strong incorporation of tritiated methyl group demonstrated that the isolated fraction contains a considerable population of particles responsive toward Erm-mediated methylation (Fig. 2B). The control reaction of Erms failed to methylate purified mature 50*S* and 30*S* subunits, confirming the fact that these enzymes act on ribosomal precursor states and accept only select substrates.

To further confirm the site specificity of the methylation and incorporation of the methylation mark onto the rRNA, we analyzed the Erm-modified ribosomal precursors using cryogenic OrbiSIMS (cryo-OrbiSIMS) (Fig. 2C and fig. S2) (*24*, *25*). Here, to establish that Erm catalyzed methylation, precursor fractions not incubated with Erm were used as a control for the study. Cryo-OrbiSIMS is a native solid-state mass spectrometry technique capable of ultrahigh mass resolution under an accuracy of 2 parts per million (ppm). Using this method, we were able to confirm that a fragment derived from 23*S* rRNA, bases 2046 to 2062 (*E. coli* nomenclature), in a native precursor ribosomal state, is being mono- as well as dimethylated [mass/charge ratio (*m/z*) changes of 14.0156 and 28.0312 Da, respectively] when incubated with Erm in the presence of SAM. To confirm that the methyl mark is effectively placed by Erm, we incubated the ribosomal precursor fraction with N6-mustard (*26*, *27*), a labile version of SAM that harbors an unstable aziridinium ring (fig. S3) (*26*). This reaction also yielded a covalent adduct (*m/z* change of 395.1917 Da) in the same rRNA fragment, thereby confirming the preferential modification of this site by Erm. Hence, results obtained from both scintillation studies and mass spectrometry strongly confirm that the precursors isolated using the U2552C point mutation serve as a substrate for Erm.

Structural characterization of the U2552C precursor fraction

To structurally probe the isolated precursor fraction, single-particle cryo-EM analysis was carried out where initial rounds of classification yielded three distinct precursor forms, termed states I, II,

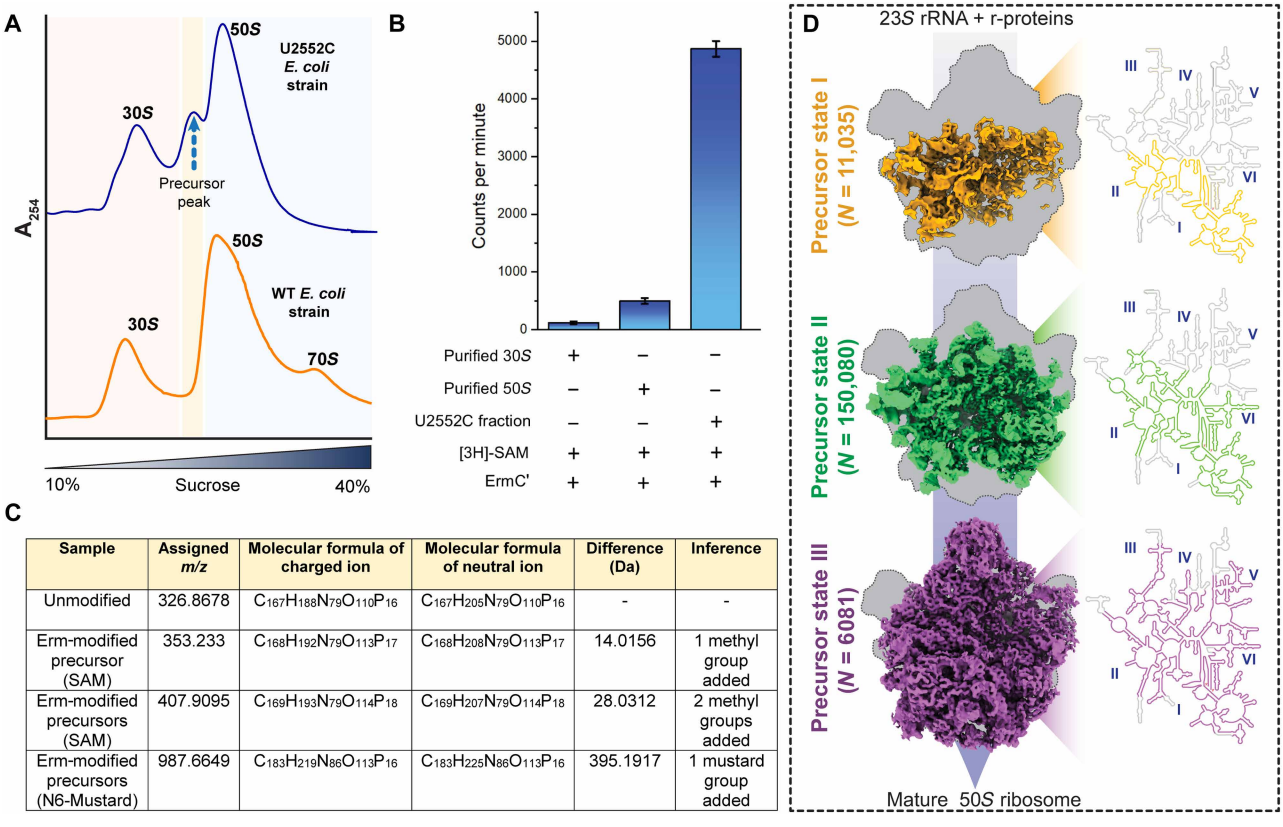

C

Sample	Assigned *m/z*	Molecular formula of charged ion	Molecular formula of neutral ion	Difference (Da)	Inference
Unmodified	326.8678	$C_{167}H_{188}N_{79}O_{110}P_{16}$	$C_{167}H_{205}N_{79}O_{110}P_{16}$	-	-
Erm-modified precursor (SAM)	353.233	$C_{168}H_{192}N_{79}O_{113}P_{17}$	$C_{168}H_{208}N_{79}O_{113}P_{17}$	14.0156	1 methyl group added
Erm-modified precursors (SAM)	407.9095	$C_{169}H_{193}N_{79}O_{114}P_{18}$	$C_{169}H_{207}N_{79}O_{114}P_{18}$	28.0312	2 methyl groups added
Erm-modified precursors (N6-Mustard)	987.6649	$C_{183}H_{219}N_{86}O_{113}P_{16}$	$C_{183}H_{225}N_{86}O_{113}P_{16}$	395.1917	1 mustard group added

Fig. 2. Sequestering ribosomal precursors which serve as substrate for Erm. (**A**) Sucrose density gradient profile shows the presence of a distinct precursor peak due to the U2552C mutation. WT, wild type. (**B**) In vitro methylation assay depicts that the precursor fractions isolated from the U2552C cells are responsive to Erm-mediated methylation however remain unresponsive to a mature 30*S* or 50*S* subunit (data from $n = 3$ independent experiments are shown where the mean has been plotted with ± SD). (**C**) Tabulated values obtained from cryo-OrbiSIMS for unmodified sample, SAM-modified samples, and N6-mustard–modified sample. The difference column shows that the additional mass (dalton) appended on to the fragment which corresponds to the modification it has undergone. (**D**) Cryo-EM reconstruction of the U2552C fraction yields three discreet precursor states referred to as states I, II, and III. Particle distribution has been provided beside each ribosomal assembly state. The 2D map of the 23*S* rRNA shown next to each precursor state demonstrates differential domain assembly in each of the states (I to VI in blue denote the domains of the 23*S* rRNA).

and III with an overall resolution of 4.5, 3.2, and 4 Å respectively (Fig. 2D). Analysis reveals that these precursor states have a diverse population distribution with state II being the most abundant. Further, the assembly intermediates showed hierarchical structuring of rRNA helices and incorporation of ribosomal proteins.

State I which resembled an early biogenesis precursor was similar to recently reported structures by Sheng *et al.* (*28*) and Qin *et al.* (*29*). Overall, this state shows the structuring of domain I and parts of domain II in the 23*S* rRNA and completely lacks the density of the three protuberances characteristic of the mature 50*S* subunit. Further, density for uL4, uL13, bL20, uL22, and uL24, the five early essential r-proteins necessary to initiate assembly, was observed along with densities of additional proteins such as bL21, uL29, and bL34 (fig. S4A).

State II was the most abundant in population and comprised 150,080 particles. This state was similar to the structure of the precursor particle obtained from YsxC-depleted strains of *Bacillus subtilis*, 41*S* in vitro reconstituted *E. coli* 50*S* ribosomal subunit intermediate (referred to as state I by authors), and an assembly intermediate obtained from RlmE knockout strain (referred to as state A-1 by authors) (*30*–*32*). Our 50*S* precursor also showed a strong resemblance to the recently reported $LiCl_2$ core particle obtained from the *E. coli* 50*S* subunit (*33*). State II shows a structured core with domains I, II, and VI, and parts of domain III assembled, whereas domain V that harbors A2058 was largely unassembled. As reported earlier, the structural organization of the core showed very little difference when compared to the core of the mature 50*S* subunit, restating the fact that the rRNA core of the larger subunit folds early on in the biogenesis process and remains largely unaltered in the mature state (*31*). The three protuberances are still absent, although it is clear that the initial structuring of rRNA has been initiated for their formation in the subsequent stages. Along with the eight ribosomal proteins reported in state I, we observed the density of an additional eight proteins (total of 16) consistent with reports for similar precursor structures (fig. S4B).

State III is the last of the three distinct states sequestered under physiological conditions as a result of the U2552C point mutation and accounts for the smallest particle distribution ($N = 6081$). State III is a late precursor particle and is characterized by the formation of the central protuberance and partial formation of the L7/L12 stalk base, whereas the density for the L1 stalk is absent. Most of the domains of the 23*S* rRNA are observed to be folded, and the incorporation of 5*S* rRNA is also seen as made evident by the formation of the central protuberance and incorporation of uL5, uL15, and uL18, the proteins essential for the integration of the 5*S* rRNA (fig. S4C) (*34*). Overall, the three states reported here show a clear stepwise organization of the rRNA and incorporation of ribosomal proteins. The assembly process of ribosomes, in vivo, occurs via parallel pathways, and the states captured here are a few discreet states among many, present in the cytosolic milieu of the cell.

Capturing the Erm–50*S* precursor complex

To delineate the precursor populations that serve as substrates for Erm, the precursor fraction was incubated with a stoichiometric excess of Erm. When the U2552C precursor fraction was mixed with Erm in the presence of the covalent adduct forming N6-mustard, only state II contained the density of Erm, indicating a preferential binding of the enzyme to this state (Fig. 3A). In state II, domain V is mostly unassembled with density observed only for regions containing H72 and H73. Density for the entire Erm protein which comprises the central Rossman N-terminal catalytic domain and the C-terminal noncatalytic domain was visible in the map with an average local resolution of 6 Å.

However, the C-terminal domain (CTD), referred to as the head of the enzyme, was relatively more ordered and displayed an average local resolution of ~4 Å. Examination of the structure revealed that it is the CTD that anchors the Erm enzyme in close proximity to the region that would have been occupied by domain V in a fully assembled 50*S* subunit. To enable this strategic docking, the CTD fits into a cleft formed by the noncanonical conformation of three rRNA helices; H95 (from domain VI), H97 (from domain VI), and partially formed H42 (from domain II) (Fig. 3, B and C). The three ribosomal helices that form a cleft accommodating Erm's CTD appear to create a complementary surface. A closer inspection of the other ribosomal precursor states captured in this study reveals that this cleft is transitory in nature and is nonexistent in state I as the three helices are yet to be assembled in early ribosomal precursors. In state II, however, the cleft has an optimal size and shape where it can accommodate Erm's CTD. As the ribosome attains maturation during the course of biogenesis, the three-helix cleft starts getting occluded by the ordering of H89 and H91, and this region becomes more compact rendering the site inaccessible to Erm. The slightly opened and flexible conformation of the three helices in state II, without the occluding effects of H89 and H91, provides a conducive environment for Erm to dock and facilitates targeting (Fig. 3D). Therefore, a dynamic ribosomal assembly intermediate where most of the domain V is still unassembled is a prerequisite for Erm to dock. This implies that Erms have a specific structurally conducive window during ribosomal biogenesis where it can methylate A2058 and induce resistance.

Since Erm is anchored to the ribosomal precursor by its CTD, we analyzed the interface for plausible motifs and potential interactions that may underlie recognition (figs. S5 and S6A). The interface between Erm's CTD and the rRNA appears enriched in positively charged and polar residues, suggestive of electrostatic and hydrogen bonding contacts. A possible point of interaction could involve helix α11 of Erm's CTD (fig. S6B); here, the stretch containing amino acids N210, N214, and H218 come in proximity of ribosomal helix 97. We speculate that N210 and N214 are positioned such that they likely form hydrogen bonds with the phosphate backbone of nucleotides A2765, A2766, and C2767, thereby stabilizing the protein-ribosome interface.

The catalytic N-terminal domain (NTD) was found to have a relatively weaker density compared to the CTD. The difference in map quality between the two domains of Erm indicated that the complex is dynamic, and the application of focused classification with signal subtraction (FCwSS) was essential for the reconstruction of Erm's density. Rigorous three-dimensional (3D) classification revealed two major classes (conformations I and II) corresponding to discrete conformations of the Erm-precursor complex (Fig. 4, A to C). In both these classes, the CTD anchor was inserted in the targeting cleft; however, the NTD showed differential conformation. It was observed that in conformation I (C-I), the anchoring of Erm brings the enzyme nearer to its cognate substrate H73 (density of H73 for C-I shown in Fig. 4D). In this conformation, we observe the presence of an additional strong density at the N-terminal end of the catalytic domain [marked by * in Fig. 4 (A and C)]. We speculate that this corresponds to a previously disordered RNA stretch that helps further anchor Erm to stabilize that NTD and aid in catalysis.

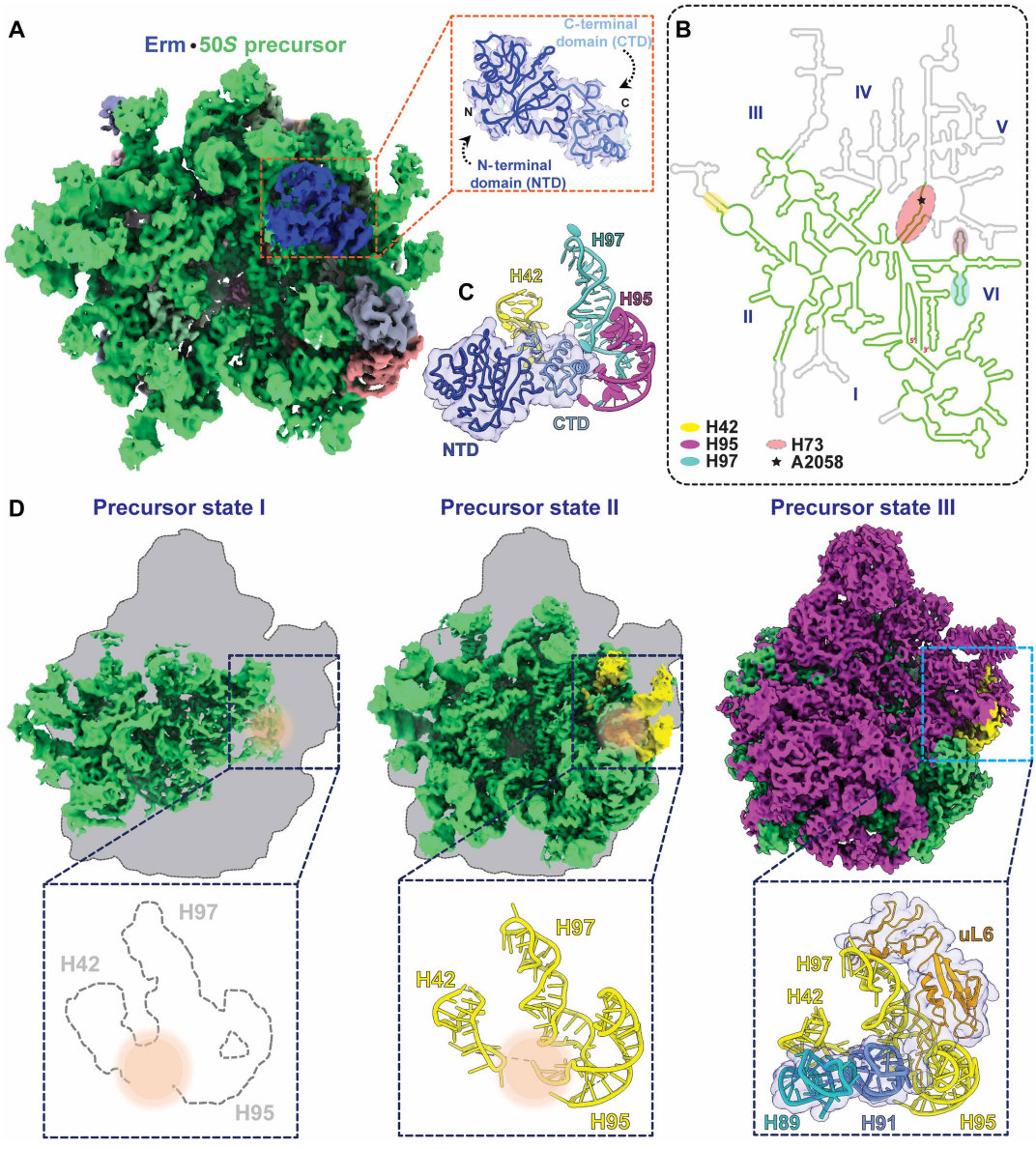

Fig. 3. Cryo-EM structure of the Erm–50*S* precursor complex. (**A**) State II (green) is the only state which shows density of ErmC′ (blue). Zoomed inset shows the complete density of Erm bound to the precursor state. The two domains of Erm, i.e., the N-terminal domain (NTD; dark blue) and the C-terminal domain (CTD; light blue), have been marked. (**B**) 2D map of the 23*S* rRNA where helices that make contact with Erm have been highlighted. Position of the target base, A2058, which gets methylated has been marked with a "★." (**C**) Erms anchor to the ribosomal precursor using their C-terminal (head) domain. The noncanonical conformation of three ribosomal helices, H42, H95, and H97, forms a complementary binding site for Erms to dock. (**D**) Comparison of the three states reveals rRNA structural determinants pertinent for Erm docking. State I lacks the folding of the three helices (absence of helices shown as dotted lines), whereas state III shows these helices (in yellow) ordered; however, additional helices such as H89 and H91 occlude the binding site of Erms, thereby preventing their docking. Only state II shows these helices freely accessible for the binding of Erms. Binding site of Erm has been shown in orange in the zoomed inset.

Further, this ordered region is in the vicinity of a positively charged patch in Erm comprising of α5 helix [shown in Fig. 4 (A and B)] and peripheral loop elements such as those connecting α3 and α4 of Erm's NTD (fig. S7). Analysis reveals that this terminal interface of Erm is found to be positively charged in various Erms isolated from different bacteria making this an apt region to dock RNA. It appears that the identified rRNA stretch likely stabilizes the Erm conformation conducive for catalysis (fig. S8). This leads us to believe that while the CTD serves as a global anchor, the terminal region of the catalytic domain containing positively charged patches serves as an rRNA-interacting stretch that guides H73 closer to the MTase. Thus, the base to be methylated, A2058 (H73), comes in proximity of the active site so that catalysis can be facilitated.

In a structurally dynamic environment such as that of a ribosomal precursor, both the CTD and NTD play a pivotal role in tethering the ends Erm and thereby impart specificity. Here, we would like to stress that tailored surface-exposed charged islands on the enzyme are an essential prerequisite for Erm-mediated methylation.

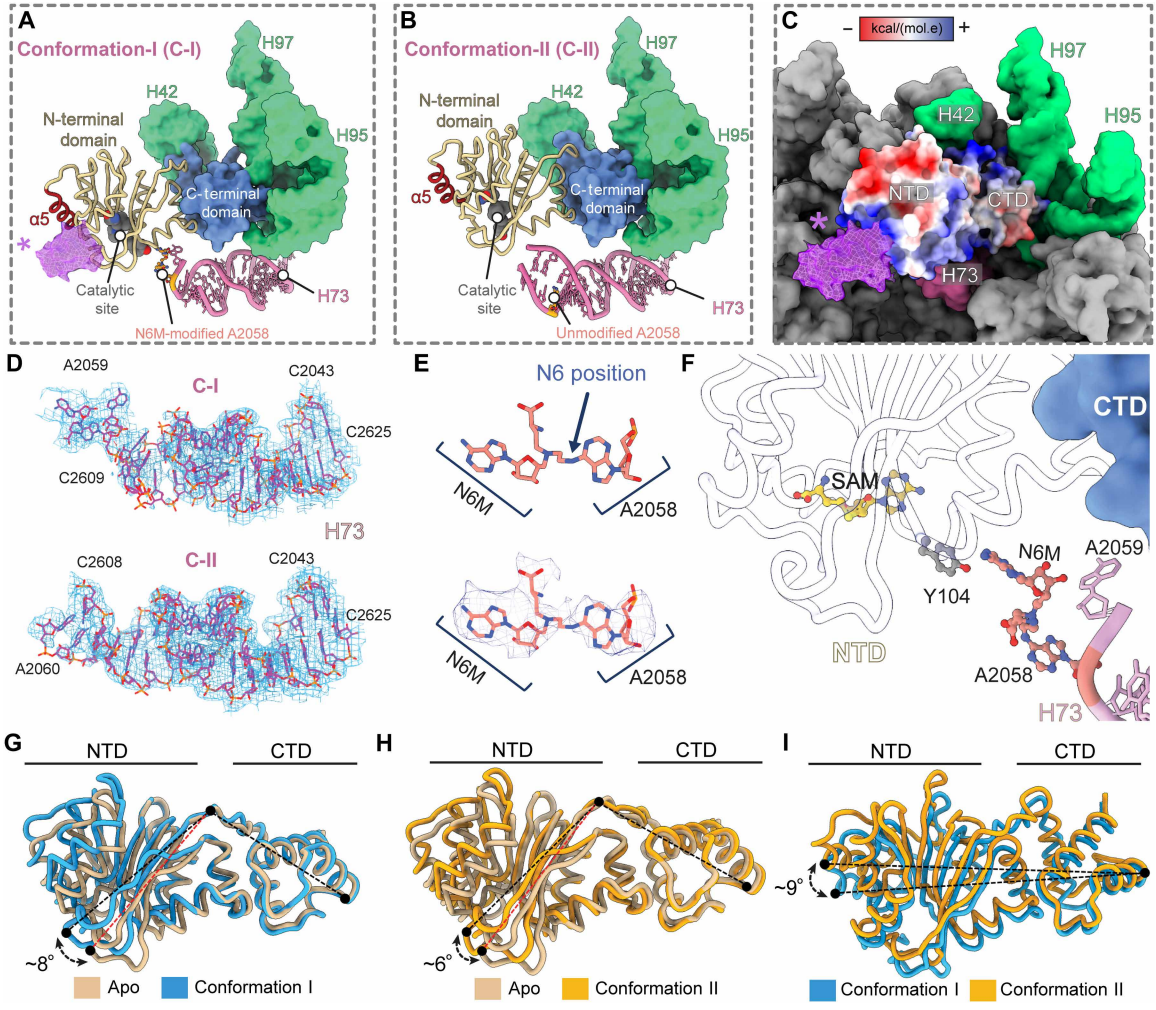

Fig. 4. Erm shows conformational flexibility when interacting with its ribosomal substrate. (**A** and **B**) Model of the two conformations of the Erm-precursor complex. (A) Erm in proximity of H73, (B) which is the state where Erm is further away from H73. The CTD of Erm has been shown in blue in surface representation, whereas the NTD is in yellow in cartoon representation. The active site of Erm in both conformations has been marked along with A2058. Helix α5 has been shown in both the conformations in maroon to mark the N-terminal positive region of Erm. (**C**) Extra density at the terminal region of the catalytic domain of Erm has been shown as a mesh (marked with *) along with the model of the C-I (the threshold for visualization is 0.0167). (**D**) Density of H73 from C-I and C-II along with the fitted model. (**E**) Density of A2058 modified with N6-mustard (N6M). (**F**) Zoomed in view of C-I showing Y104 and N6-mustard adduct. Coordinates of SAM from PDB ID: 1QAN has been superimposed to show the putative SAM binding site. (**G** and **H**) Comparison of the Erm structure in C-I and C-II with Apo form (PDB: 1QAM) showing interdomain reconfiguration. (**I**) Superimposition of the Erm model in both conformations shows a hinged motion of approximately 9°.

Moreover, a rigorous analysis of the cryo-EM complex reinstates that we have captured an active form of the Erm-precursor complex, as A2058 was found to contain extra density corresponding to the mustard group attached to the N6 position as an adduct (Fig. 4E). Here, as the incorporation of a methyl group via SAM is too small a mark to be identified at our resolution, strategic utilization of the SAM analog was instrumental in visualizing Erm-based modification, asserting the functional relevance of the complex. Further, we find the adenine of N6-mustard after adduct formation to be anchored via Y104, a conserved aromatic amino acid in the catalytic site of the enzyme (Fig. 4F). Y104 represents one of the key residues in N6 MTases and plays a crucial role in directing the target base into the active site by assisting in a near 180° flip allowing methylation to occur (*17*). Y104 is prone to conformational flexibility, where it guides the target adenine into the active site during the course of the reaction and thereafter flips out as the base exits the catalytic pocket (*35*). Thus, the captured cryo-EM class, C-I, represents a complex where the rRNA along with N6-mustard is trapped while exiting the active site after complexation. The second captured class, C-II, has the NTD retracted further away from H73 (density of H73 for C-II shown in Fig. 4D). Even the previously observed RNA stretch at the N-terminal end of the enzyme appears to be substantially disordered in the map density. However, the CTD in C-II remains docked in its three-helix cleft. We also observe that Y104 appears to have an alternate conformation compared to C-I (fig. S9, A to C). This is in line with the proposed mechanistic role of this conserved aromatic residue in N6 MTases (fig. S9C) where it undergoes differential orientations based on its proximity to the target base. Furthermore, comparison of H73 in C-I, C-II, and the mature 50*S* (fig. S10) showed considerable conformational flexibility especially near the region

which harbors A2058. Here, A2058 appears to have shifted by ~11 Å in C-I when compared to its position in C-II and by ~17 Å in opposite direction with respect to C-II in the mature 50*S* form (fig. S10). These observations point toward the dynamic nature of the NTD-H73 interaction where Erm induces a transient reorganization of the target helix.

Further, a comparison of the crystal structure of ErmC′ [apo form, Protein Data Bank (PDB) ID: 1QAM] with the substrate-bound state indicates a conformational rearrangement of the two domains, where the CTD and NTD move farther from each other (Fig. 4, G and H) (*36*). This interdomain movement likely allows Erm to take on a favorable configuration conducive to orient itself appropriately when interacting with its dynamic precursor substrate. For both C-I and C-II conformations of the Erm–ribosomal precursor complex, one where Erm's NTD is distant from H73 while docked at its CTD, and the other where Erm's NTD is in proximity to H73 and sandwiched at both the NTD and CTD, a hinge motion is observed. A comparison of the two states revealed a molecular hinged motion of the NTD by ~9° relative to the rigidly docked CTD (Fig. 4I). These observations highlight that the domains of Erm independently play a role in substrate recognition and conforms in response to the surrounding environment. Thus, the enzyme appears to have evolved to develop a locator domain (CTD) that anchors Erm near the vicinity of the substrate helix (H73), whereas the catalytic domain (NTD) scans for H73, thereafter positioning it appropriately for methylation.

smFRET reveals dynamic interactions of the Erm–50*S* precursor complex

To establish the dynamic nature of the Erm–50*S* precursor complex, we performed smFRET measurements which enabled us to probe the subtle motion of Erm at the molecular level. First, we engineered a system with modified 50*S* precursors by site-specific alternation of H39 in domain II of the 23*S* rRNA (fig. S11A). On the basis of structural insights from the cryo-EM maps of the precursor state II, H39, an ordered part of the precursor and ~5 nm from the methylation site (H73), was labeled with the donor probe Cy3 (*37*, *38*). To enable fluorophore tagging, H39 was modified to include a hairpin of known sequence, and a complimentary oligonucleotide strand containing Cy3 was later annealed to produce a fluorescently tagged precursor variant that can be probed via smFRET. To incorporate the acceptor probe (Cy5) at specific sites within Erm, cysteine residues in the NTD and CTD were used to conjugate the dye individually to the domains using maleimide chemistry [see Materials and Methods and fig. S11 (B and C)] (*39*). Using these donor- and acceptor-tagged systems (Fig. 5A), we performed smFRET measurements on surface-tethered Erm-precursor complexes via a total internal fluorescence (TIRF) microscope (see Materials and Methods and fig. S12). The acquisition of FRET time trajectories on individual complexes allowed us to evaluate FRET efficiency (E_{FRET}) distributions and thereby probe the dynamic conformational landscape of Erm-bound precursor ribosomes.

Conjugation of Cy5 onto the CTD yielded FRET trajectories that consistently showed a transition between a no-FRET to a single, high-efficiency state (Fig. 5B and fig. S13A). Analyses of 1203 such trajectories reveal a unimodal E_{FRET} distribution centered at 0.68 ± 0.05 (Fig. 5C), which corresponds to an interfluorophore separation of 4.8 ± 0.2 nm. This estimate of distance is consistent with the CTD of Erm being docked at the ribosomal precursor's three-helix cleft as observed from cryo-EM reconstructions (Figs. 3C and 4, A and B). In contrast, smFRET traces of NTD-tagged Erm-precursor complex reveal transitions between multiple states (Fig. 5D and fig. S13B) indicative of the underlying dynamics of this domain when bound to the ribosome. (Fig. 4, A and B). E_{FRET} distribution for Cy5-labeled NTD exhibits three discernible populations, centered at 0.38 ± 0.09 (F-I), 0.54 ± 0.04 (F-II), and 0.77 ± 0.08 (F-III) (Fig. 5E, a). We note that the estimated interfluorophore distance for F-II (5.3 ± 0.1 nm) aligns closely with the spatial separation between H39 and NTD of Erm in the C-I cryo-EM structure (~5 nm) (Fig. 4A), where NTD is near to the methylation site. In contrast, F-I (6.2 ± 0.4 nm) corresponds to a conformation where NTD moves away from H39 and is consistent with the distance (~6 nm) between H39 and NTD likely representing cryo-EM state C-II (Fig. 4B). No state representing F-III (4.3 ± 0.2 nm) could be mapped to any of the cryo-EM reconstruction. However, after analyzing the possibilities using the cryo-EM precursor complex, as a guide, we believe that it may represent a state where NTD sways toward H39 closer to the ribosomal core. It was noticed that F-II harbors relatively higher population indicative of a stable conformation compared to the other states. This can perhaps be associated with favorable electrostatic interactions between the positively charged terminal patch of NTD (fig. S7) and the RNA stretch which becomes relatively ordered in C-I (F-II corresponding state) when Erm is in proximity of its target.

Most trajectories display transitions only between two of these three states, and transitions involving all three states are rare (~4% of traces) (fig. S13B, top). We therefore analyzed subpopulations of the trajectories based on transitions between any pair of the three conformations represented by E_{FRET} states (F-I, F-II, and F-III). The resultant E_{FRET} distributions (Fig. 5E, b to d) reveal that most transitions occur between the states F-II and F-I or between F-II and F-III, highlighting the central role of F-II in the conformational landscape. This inference is further substantiated by both the transition density plot (TDP) (Fig. 5F) and dwell time analyses (fig. S14), which point to F-II being the major hub while having the lowest exit rate. The above observations indicate prevalence of a swaying motion of NTD—oscillating between distal and proximal positions relative to H39 (Fig. 5G). Here, F-II, representing a catalytically poised intermediate, stabilized by transient ribosome contacts, whereas the other two conformations represent noncatalytic states. Overall, the CTD holds the entire protein in position to prevent it from dislodging and allows for fine-tuning of the spatial orientation of the catalytic domain to seek out the target base in a dynamic environment presented by the precursor. These observations suggest that the NTD samples distinct conformations, an important aspect enabling the enzyme's flexibility in a constantly evolving ribosomal environment, thereby ensuring effective methylation. Thus, our integrated approach, combined smFRET and cryo-EM analysis, elucidates a comprehensive picture of the overall targeting and catalytic recognition mechanism of Erm within the ribosomal precursor.

DISCUSSION

Nucleoside methylation is ubiquitous and plays a crucial role in regulating key biological processes, such as transcriptional regulation via epigenetic modification of CpG islands in DNA (*40*). MTases also actively participate in RNA methylation, where they are essential for processes such as splicing, nuclear export, tRNA functionality, and ribosome biogenesis (*13*, *41*, *42*). Owing to it being a relatively stable mark, pathogenic organisms have also adopted methylation

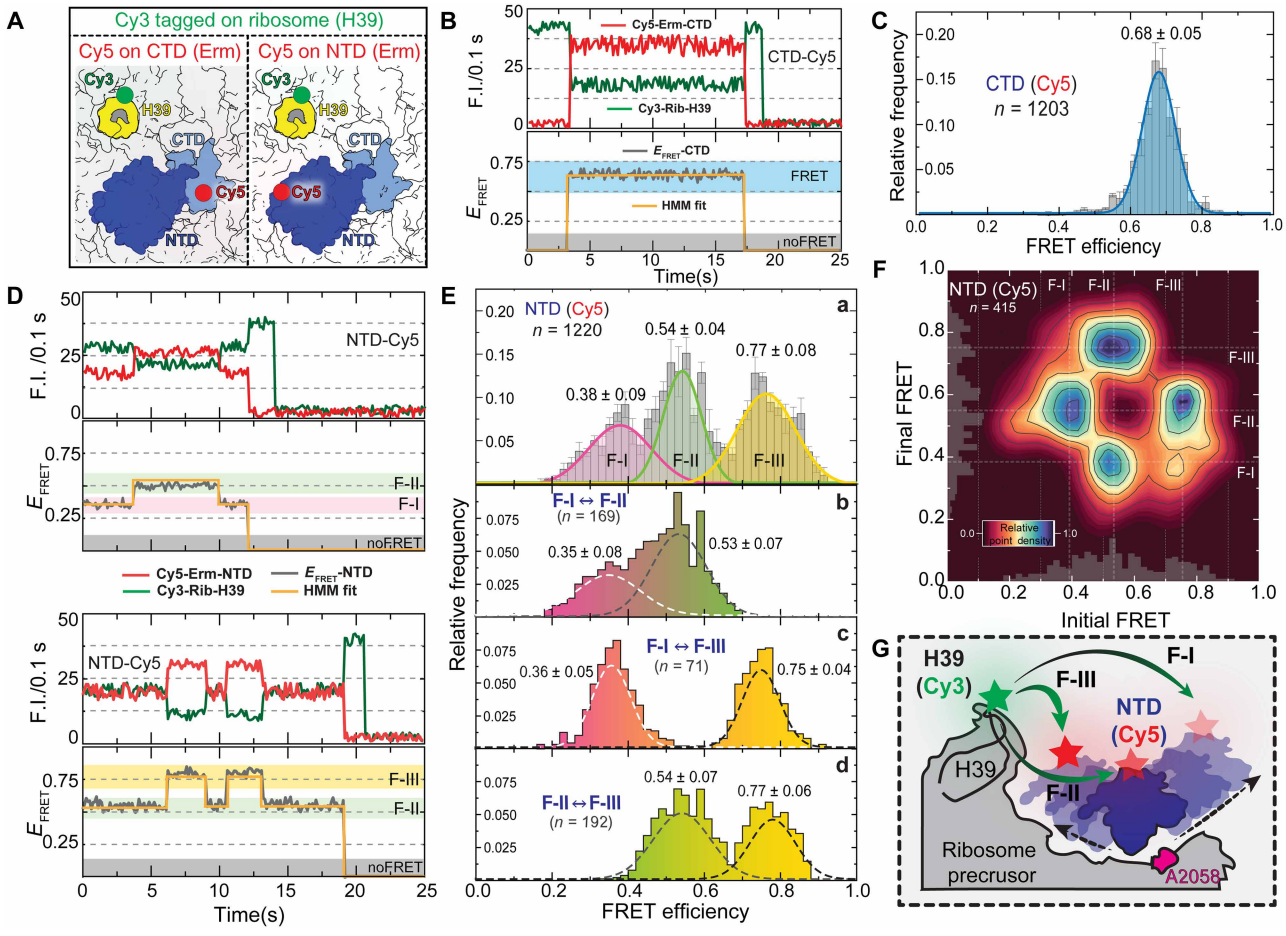

Fig. 5. Single-molecule FRET analysis of Erm dynamics with ribosome precursor state II. (**A**) Schematic of Cy3/Cy5 labeling sites within ribosome precursor–Erm complex. (**B**) Representative single-molecule fluorescence traces of Cy3-labeled ribosome precursor paired with Cy5-labeled Erm (CTD), showing distinct donor/acceptor signals alongside smFRET trace [F.I. - Fluorescence Intensity (counts/ 0.1s)]. (**C**) FRET efficiency histogram for CTD-labeled Erm, fit with a unimodal Gaussian distribution, indicating a single stable state (E_{FRET} = 0.68 ± 0.05). (**D**) Representative traces for Cy5-labeled Erm (NTD), revealing dynamic multistate behavior. (**E**) (a) FRET efficiency histogram for NTD-labeled Erm, fitted with multimodal Gaussian distribution revealing three states (F-I, F-II, and F-III). (b to d) FRET efficiency histogram of traces after trace deconvolution depending on transitions between specific states (F-I ↔ F-II, F-I ↔ F-III, and F-II ↔ F-III). (**F**) Transition density plot (TDP) for NTD-labeled Erm, illustrating preferred transitions between the E_{FRET} states. (**G**) Model of the Erm-ribosome precursor interaction dynamics from smFRET, visualized from the NTD, the CTD is not visible [number of traces analyzed (*n*) indicated on the panels].

as a means to induce antibiotic resistance. However, for optimal activity, the ability to appropriately target its substrate is a prerequisite as even if the enzyme has a catalytically competent domain, it needs to recognize and access the correct substrate. Structural analysis of several MTases reveals that many of them have evolved appendages that are located either on the C- or N-terminal end of the catalytic Rossman fold domain. These unique auxiliary domains are tailored to recognize the substrate classes they catalyze and ensure effective targeting (Fig. 6). Truncation of these targeting domains or mutation of critical residues situated in them often results in a diminished or abolished methylation activity. An instance of this is seen in the case of TlyA (O-MTase) and RmtC (N-MTase) which confer resistance against capreomycin and aminoglycosides such as kanamycin and gentamicin, respectively, where mutations introduced in the NTD of TlyA of RmtC greatly impair their methylating ability (*43*, *44*). A similar requirement of peripheral targeting domains has also been observed in the 28*S* biogenesis factor ZCCHC4, where mutations or truncations in its CCHC, C2H2, and GRF domains led to a marked reduction in enzyme catalysis (*45*). Similarly, $tRNA^{Phe}$ methylating TrmN contains an evolutionarily conserved THUMP (thiouridine synthase, MTase, and pseudouridine synthase) domain required for methylation (*46*). Apart from these, there remain several other examples that highlight the critical role of noncatalytic structural elements in governing the efficiency and specificity of methylation across diverse classes of MTases.

In the case of Erms, we demonstrate that substrate targeting is integral to methylation. Here, the CTD (also referred to as head domain) is crucial for recognition. Erm is a unique example where, unlike several other MTases, it accesses a dynamic precursor state of the 50*S* ribosome. This makes the role of targeting even more important because it acts on a transient substrate state that has fleeting structural features. Here, both the timing of methylation and precision of the targeting are paramount factors for catalysis. Structural characterization of such MTase in action has been difficult as isolation

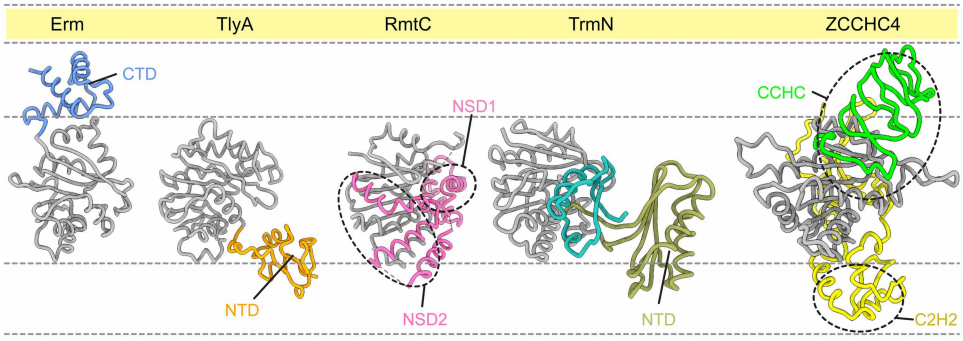

Fig. 6. Comparison of MTases with Rossman fold. In each protein, the Rossman fold containing catalytic domain has been aligned and colored gray, while other additional domains have been colored differently. GRF domain of ZCCH4 has not been labeled for the sake of clarity. NSD, N-terminal subdomain. PDB IDs used: 1QAM, 1PQB, 7S0S, 3TMA, and 6UCA.

of the target substrate itself is particularly challenging. Thus, several MTases that typically access precursor states, such as those partaking in ribosomal biogenesis or in conferring resistance, remain poorly characterized. The cryo-EM structure presented in this work addresses a longstanding question regarding the physiological substrate of Erm and how the enzyme engages with it. We show that Erm acts in a specific, structurally permissive window during ribosome assembly, wherein sequestration of a 50*S* precursor state—referred to as state II—allows stable trapping of the Erm-precursor complex. While prior cryo-EM and crystallographic studies have captured ribosomal MTases (r-MTases) bound to mature or near-mature bacterial ribosomal subunits (*43*, *44*, *47*, *48*), our structure represents a resistance-associated MTase bound to a relatively early prokaryotic ribosomal assembly intermediate.

Further, structural comparison of Erm in its apo and ribosome-bound forms reveals a key role for the connector loop, which mediates conformational changes between the NTD and CTD, enabling effective docking onto the ribosome. This suggests that while the NTD is capable of independently engaging and methylating its RNA substrate, it depends on conformational cues provided by the CTD to trigger catalysis. In this case, the CTD clasps a tertiary RNA architecture located at a distal position of the ribosome (formed by parts of domains II and VI). The transient three-helix–CTD complex initiates breathing helping NTD to scout for its cognate substrate, in the mostly unassembled domain V. Consequently, as reasserted by single-molecule studies, CTD is relatively less dynamic, corroborating the role of this domain in anchoring Erm to the targeting site. Whereas the NTD, as pointed out by both cryo-EM reconstructions and smFRET analysis, exhibits conformational dynamics. The partially unstructured nature of the ribosomal precursor, particularly domain V, where H73 and the target base A2058 reside, undergoes active assembly. Thus, the Erm connector loop allows NTD to adjust, allowing the domain to sway and effectively scout for its substrate during the catalytic window. The NTD appears to "search" for its target through a combination of electrostatic interactions via its N-terminal positively charged surface patch (this work) and is likely aided by directing loop elements, as shown in previous reports. Together, our data suggest a division of function between the two domains of Erm: The CTD governs global positioning and stable association with the ribosome, while the NTD carries out local target search and catalysis. Notably, the swaying motion of the NTD, rather than complete enzyme dissociation, may facilitate successive methylation events at the target base, allowing for efficient exchange of SAM and release of the hydrolyzed cofactor. This mechanism may represent a strategy among dimethyltransferases to achieve consecutive methylation while bound to their substrates.

The importance of Erm's CTD in substrate targeting is further underscored by biochemical experiments, where a CTD-deleted version of KsgA (paralog of Erm) exhibited a ~50% reduction in methylation efficiency when incubated with the 30*S* subunit (*47*). Early studies on ErmC′ similarly demonstrated that cells transformed with Erm constructs lacking the CTD failed to confer resistance to macrolides (*49*). Maravić and colleagues (*49*) hypothesized that the CTD's role was restricted to promoting proper folding of the catalytic domain, with no direct involvement in substrate targeting, However, as evident through our work, the domain is paramount toward providing specificity. The importance of the CTD is again highlighted in Erm37, a headless variant found in *Mycobacterium tuberculosis*, which is unable to demonstrate effective targeting and is promiscuous nature (*50*). On the basis of these observations, we propose a model for Erm-mediated resistance (Fig. 7), integrating both targeting specificity and dynamic conformational changes.

It appears that apart from shape complementarity, surface electrostatic potential of r-MTases also plays into its function. When compared with KsgA, the closest evolutionary counterpart of Erm, we observe that, unlike Erm, KsgA has a dedicated positively charged surface for extended recognition (Fig. 8). One face of KsgA is enriched in positively charged residues, while the opposite side is enriched in acidic residues. Thus, the sequestered surface charge of KsgA allows it to preferentially interact with one of its faces with the 30*S* subunit as opposed to the other. Since KsgA methylates a nearly mature form of 30*S* (*47*, *51*, *52*), a more defined substrate, it exploits the entire surface to correctly position itself and orient such that it interacts with multiple helices enabling the methylation of the target helix, h45. On the contrary, Erm enters at a relatively early stage of ribosomal biogenesis where several structural features of the ribosome are transitory. Thus, Erm primarily uses the CTD to dock and the NTD's surface positive patches help direct H73 toward the methylation pocket. Once A2058 is in proximity, loops 1 and 12 likely help in identifying local structures that allow the rRNA segment to fit for effective catalysis (*14*). These observations highlight how MTases tailor their surface charge distribution to create complementary electrostatic landscapes for substrate RNA and the surrounding targeting elements.

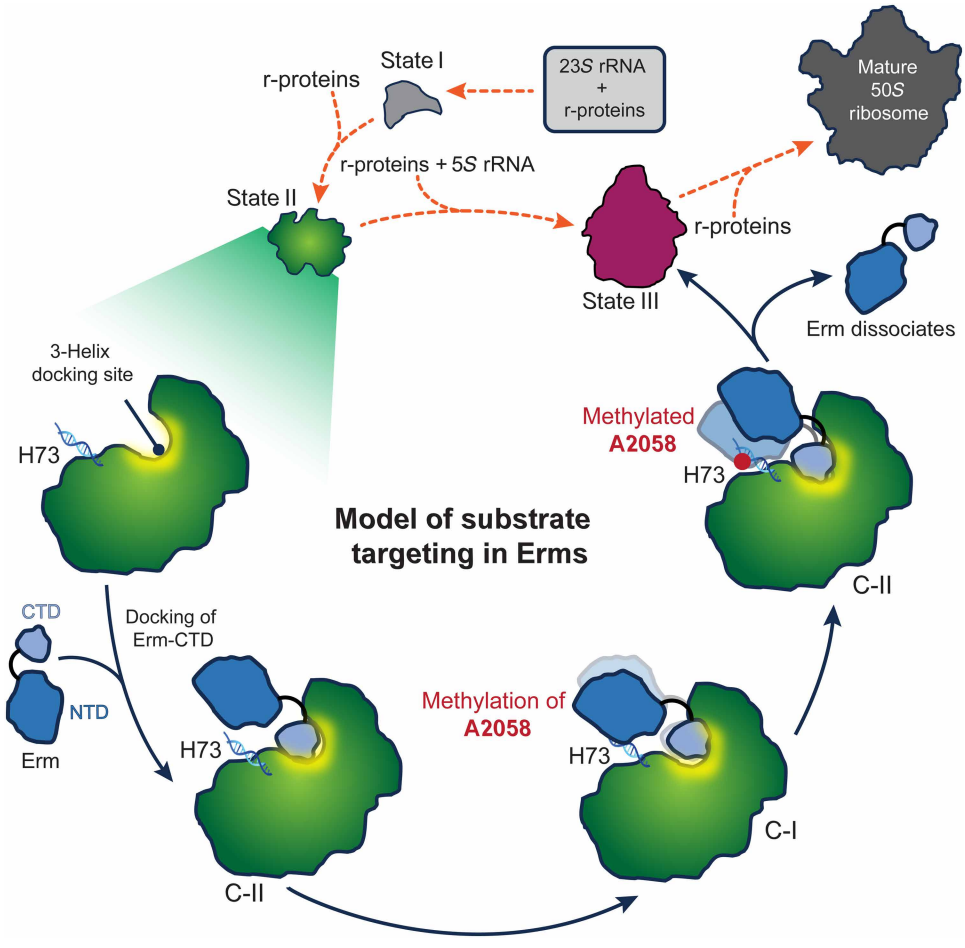

Fig. 7. Schematic of proposed model of Erm-mediated 50*S* precursor methylation. Erms are able to bind to a specific state of the ribosomal precursor where the target helix, H73, is exposed. Erm's CTD, responsible for global recognition, docks into a transient cleft formed by H42, H95, and H97. At this stage, the NTD or the catalytic domain is further away from H73 (C-II). Subsequently, conformational swaying-like motion in Erm allows its NTD to locally scan for the target base and come in proximity of H73 to facilitate methylation (C-I). Followed by which, Erm retracts and dissociates from the precursor, and the immature ribosome follows its course of biogenesis.

In conclusion, this study provides an avenue for drug development toward specific inhibitors for the Erm family of enzymes. Previous attempts have been made to target Erms by the development of small-molecule inhibitors with several of them directed toward the catalytic domain or the connected SAM binding domain (*53*–*56*). However, the conservation of the active site and SAM binding sites between Erms and other housekeeping Rossman fold–containing MTases leads to high chances of cross-reactivity. This work emphasizes the importance of noncatalytic structural elements—particularly those governing substrate recognition—as promising targets for selective inhibition. The Erm family of enzymes demonstrates very similar 3D architecture (fig. S15) with relatively low sequence similarity in the head domain (*36*, *57*–*59*). We, therefore, propose that targeting this region represents a viable strategy for designing specific inhibitors, opening avenues toward strategies that resist resistance.

MATERIALS AND METHODS

Construction and purification of U2552C 23*S* rRNA mutant

The U2552C mutation in the 23*S* ribosomal DNA containing p278MS2 plasmid (gift from R. Green, John Hopkins University, USA) (*60*) was introduced using an EZchange Site-directed Mutagenesis kit following the manufacturer's protocol. The mutation was confirmed by sequencing, and the mutant plasmid was transformed into *E. coli* DH5α cells to overexpress and purify it. To express the ribosomes containing the U2552C mutation, the mutated plasmid was transformed into MC338 strain (a gift from G. Culver, University of Rochester, Rochester, New York, USA) (*61*).

The U2552C_MC338 strain was grown in LB media at 30°C until optical density at 600 nm (OD_{600}) reached 0.4 to 0.5. The cells were harvested and resuspended in ribosome buffer [20 mM tris-Cl (pH 7.5), 100 mM NH_4Cl, 10 mM $Mg(OAc)_2$, and 6 mM 2-mercaptoethanol] and disrupted by sonication. After incubating the lysate with deoxyribonuclease I (10 μg/ml) for 10 min, cell debris were removed by centrifugation at 15,500*g* for 30 min at 4°C. Ribosomal particles were pelleted down by layering the supernatant on top of 1.1 M sucrose cushions made in a buffer containing 20 mM tris-Cl (pH 7.5), 500 mM NH_4Cl, 10 mM $Mg(OAc)_2$, and 6 mM 2-mercaptoethanol and centrifuged in a 70Ti (Beckman and Coulter) rotor at 140,900*g* for 16 hours at 4°C. The resulting glassy pellet was rinsed with the above-mentioned ribosome buffer and resuspended in the same. 70*S* ribosomal particles were dialyzed in a dissociation buffer [20 mM tris-Cl (pH 7.5),

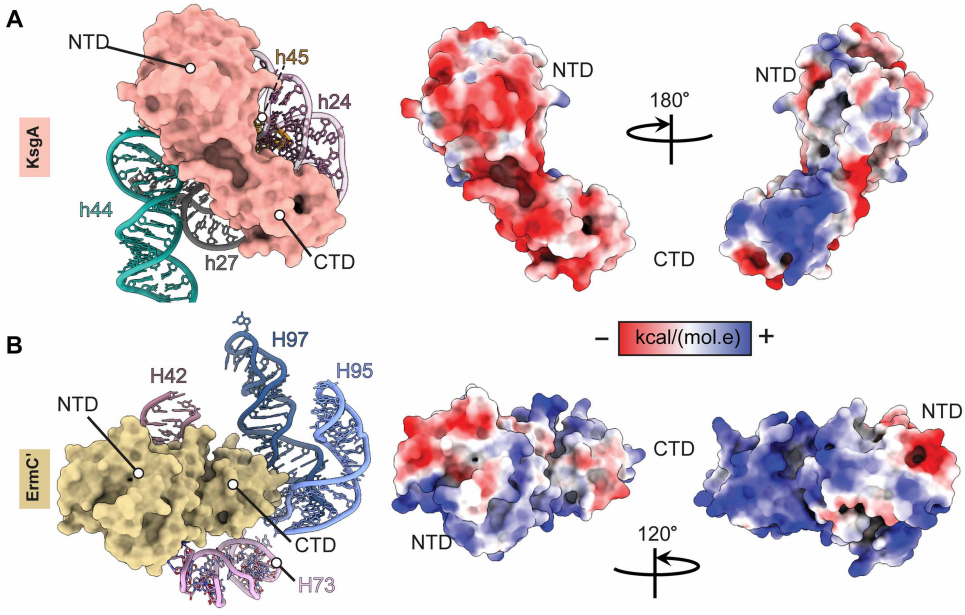

Fig. 8. Comparison of the mode of binding of Erm with KsgA. (**A**) Model of KsgA bound to the platform region of the 30*S* ribosomal subunit. KsgA has been shown in surface representation, and the 16*S* rRNA helices have been shown in cartoon representation. Surface potential representation of KsgA shows the protein to have a dedicated positive patch on the side which interacts with RNA. (**B**) Model of Erm bound to the 50*S* precursor state. Erm has been shown in surface representation, while the 23*S* rRNA helices have been shown in cartoon representation. Unlike KsgA, Erm does not have a dedicated positive surface patch rather a diffused one.

150 mM NH_4Cl, 1 mM $Mg(OAc)_2$, and 6 mM 2-mercaptoethanol] to separate ribosome into its corresponding subunits. The dialyzed crude extract was separated by zonal sedimentation in 10 to 40% sucrose gradients (SW32-Ti rotor at 59,700*g* for 16 hours at 4°C). The gradients were fractionated using a Gilson fractionator in a BioComp station, and fractions corresponding to mature 30*S*, mature 50*S*, and 50*S* precursors were collected and dialyzed against a storage buffer [20 mM tris-Cl (pH 7.5), 150 mM NH_4Cl, 1 mM $Mg(OAc)_2$, and 6 mM 2-mercaptoethanol]. Dialyzed 50*S* precursor fractions were concentrated up to 2 μM. The concentrated precursor was checked on a 2% agarose gel for rRNA integrity and stored in aliquots at −80°C until further use.

Purification of Erm enzymes

ErmC′ gene was previously cloned from *B. subtilis* BD1167 (a gift from D. Dubnau, Rutgers University, Newark, DE, USA), and Erm42 was cloned from *Pasteurella multocida* (a gift from S. Douthwaite, University of Southern Denmark, Denmark) both of whose expression and purification were performed as described previously (*49*, *62*).

Scintillation assay

Scintillation assay or in vitro methylation assay was done according to previous reports (*47*). Briefly, the assay was performed in a methylation buffer [20 mM tris-HCl (pH 7.5), 80 mM NH_4Cl, 1 mM $Mg(OAc)_2$, and 6 mM 2-mercaptoethanol] containing 0.3 μM mature 30*S*, mature 50*S*, or ribosomal precursor, 0.3 μM MTase, 0.1 μM (3H)-SAM (100 Ci/mmol, American Radiolabeled Chemicals), and 1 U of ribonuclease inhibitor (Thermo Fisher Scientific) in a total reaction volume of 30 μl. Reactants were mixed and incubated at 37°C for 50 min in the buffer described above. After 50 min, 10 μl of ice-cold 5% trichloroacetic acid (TCA) was added, to quench the reaction. The quenched reaction was deposited on a precharged membrane (Nylon 66 filter membrane), washed extensively with chilled methylation buffer supplemented with 5% TCA, and rinsed briefly with 100% ice-cold ethanol. The filter paper was air dried for 30 min and then placed into 2 ml of scintillation liquid (Ultima Gold, PerkinElmer). Radioactivity was counted using our in-house scintillation counter (Tri-Carb B2810TR; PerkinElmer, USA).

Cryo-OrbiSIMS sample preparation, data collection, and analysis

Cryo-OrbiSIMS experiments were performed as previously described (*24*, *25*). Samples were adsorbed as a hydrated monolayer on a gold substrate, washed with phosphate-buffered saline, and immediately flash frozen by plunge freezing in liquid nitrogen. OrbiSIMS data were collected under cryogenic conditions at −150°C. For each sample, data were collected in negative polarity mode in three replicates. Two replicates were also collected for the gold substrate and were used as reference spectra for data processing. Single beam 20-keV Ar_{3000}^+ with an Orbitrap Q Exactive analyzer was used for all measurements, and the current of the primary beam was 230 pA, total ion dose of 3.65×10^{13} ions/cm^2 and probed surface area of 200 μm by 200 μm. Mass calibration of the Q Exactive instrument was performed once a day using silver cluster ions. Electron flood gun and argon gas flooding were used for charge compensation, and the target potential was set to −57 V. For all Orbitrap data, mass spectral information was collected in a range *m/z* 150 to 2250. The mass resolving power of the Orbitrap analyzer was set to 240,000 at *m/z* 200.

IonToF SurfaceLab 7 was utilized to extract peak lists from the raw spectra. Subsequent analysis of the peak lists was carried out using MATLAB 2021a using custom codes as previously described (10.5281/zenodo.10960750). Peak assignments were performed by comparing the experimental *m/z* values to a database of theoretical calculations for all the possible fragments generated from the 23*S*

rRNA sequence with a 2-ppm error. To compensate for the computational cost of generating the theoretical database, a targeted assignment strategy was used to prioritize assignment of unique fragments of increasing lengths centered on A2058 in the 23*S* rRNA sequence.

Preparation of N6-mustard SAM

N6-mustard SAM was prepared using a reported literature procedure. We initiated the preparation of N6-mustard SAM (fig. S16) with the protection of hydroxyl groups of adenosine **1** using acetone and p-toluenesulfonic acid to afford compound **2** in 92% yield. The hydroxyl group of the 5′ positions was converted to phthalimido derivative to get compound **3** in 60% yield. The acetonide group in compound **3** was selectively deprotected using trifluoroacetic acid:H_2O:tetrahydrofuran (3:1:1, v/v/v) to afford compound **4** in 55% yield. The 3′,2′-hydroxyl groups of compound **4** were protected using *N*-tris(hydroxymethyl) methyl-2-aminoethanesulfonic acid–Cl and imidazole in *N*,*N*′-dimethylformamide to furnish compound **5** with a 62% yield. The phthalimido group of compound **5** was reduced to amine to obtain compound **6** in 70% yield. Compound **6** was subjected for the reductive amination using aldehyde **7** and $NaCNBH_3$, in methanol to afford compound **8** in 52% yield. Then, N-alkylation of compound **8** was carried out using bromoethanol and N,N-Diisopropylethylamine (DIPEA) in toluene to furnish compound **9** in 50% yield. Last, compound **9** was subjected to iodination using PPh_3 and I_2 in dichloromethane (DCM) to afford compound **10**, which was further subjected to deprotection of acid labile protecting groups using 4 N HCl in dioxane (1:1, v/v) in DCM to get the desired compound N6-mustard SAM **11**. All the compounds were characterized using nuclear magnetic resonance, and high resolution mass spectrometry (HRMS) and the data was matched with those reported in the literature (*26*, *27*, *63*).

Grid preparation of Erm–50*S* precursor complex

The purified U2552C fraction and Erm were mixed in a stoichiometric ratio of 1:10 along with the addition of N6-mustard (*26*, *27*, *43*, *44*) (fivefold excess of protein concentration) and incubated at 30°C. Three microliters of the mixture was applied to a glow discharged Quantifoil holey carbon grid (R 1.2/1.3, Cu 300 mesh) at a precursor concentration of 1 μM on a Vitrobot Mark IV (Thermo Fisher Scientific) set at 4°C and 100% humidity with no wait time, blot force of 6, and 3.5-s blot time. The grids were screened for good quality ice, particle distribution, and density in a Talos L120C transmission electron microscopy (TEM) operated in cryo-mode, and images were collected at a magnification of ×22,000 with a defocus value of −3 μm. Data used for image reconstruction were collected on a Krios G4 cryo-TEM having a Gatan K3 direct detector equipped with a BioContinuum energy filter. Movies were collected in super-resolution counted mode at a magnification of ×64,000 having a calibrated pixel size of 0.69 Å, exposure of 2 s with a total dose of 41.25 $e^-/Å^2$ over 40 frames (1.03 $e^-/Å^2$ per frame). A defocus range of −0.75 to −2.5 μm was used, and 3700 movies were collected.

Erm–50*S* precursor complex data processing

Image processing was done using RELION 4.0.1. Three thousand seven hundred movies were split into two sets, one containing 2000 movies and the other having 1700 movies. Each of the sets was individually corrected for beam-induced motion using the RELION's inbuilt algorithm using a 5 by 5 patch configuration. The contrast transfer function (CTF) for the aligned micrograph sets was estimated using CTFFIND4.1.14. A total of 909,607 and 792,947 particles were picked from sets 1 and 2, respectively, using templates defined from a subset of the micrographs. The particles were extracted using a box size of 480 pixels (~330 Å) and were binned twice to speed up processing. The binned extracted particles were subjected to several rounds of 2D classification ($T = 2$) with a mask diameter of 280 Å, and classes resembling 50*S* precursors were selected which composed of 115,780 and 104,927 particles from sets 1 and 2, respectively. The particle star file from each set was joined and subjected to 3D classification (class = 10, $T = 4$). After inspecting the classes in ChimeraX (*64*), classes which resembled a 50*S* precursor structure were selected. A total of four classes were combined and further subjected to 3D refinement and postprocessing. The particles from 3D refined classes were used for estimation of per-particle defocus, beam-tilt, aberration, and anisotropic magnification estimation followed by refinement and Bayesian polishing. The B-factor weighted particles were further 3D refined and were subjected to 3D classification without alignment (class = 5, $T = 20$).

On inspection in ChimeraX, classes 1 and 4 contained precursor particles with the density of Erm, while classes 3 and 5 were two other states of ribosomal precursors comprising 11,035 and 6081 particles, respectively. Classes 3 and 5 were subjected to 3D refinement followed by CTF refinement and Bayesian polishing and sharped to yield maps of 3.4 and 3.2 Å, respectively (lowpass filters of 4.5 and 4 Å were applied for visualization purposes). Classes 1 and 4 were merged (total of 150,080 particles), extracted with 2× binning, and refined to yield a map of 3.2-Å resolution. Although we were able to capture a strong density for the CTD of ErmC′, the NTD was of considerably lower resolution. Therefore, a focused 3D classification was performed with signal subtraction without alignment (FCwSS) with $T = 200$. A partial signal subtraction of the cryo-EM density corresponding to the ErmC′ from the refined particles was carried out, and FCwSS was performed by classifying into four classes. Classes 1 and 3 with 64,804 (43%) particles showed fragmented cryo-EM density. Class 2, with 29,668 (20%) particles, contained Erm's NTD in close proximity to the target rRNA strand. Class 4, with 55,608 (37%) particles, contained Erm in a slightly different conformation where its catalytic domain was slightly away from the substrate rRNA strand. Classes 2 and 4 were subjected separately for 3D refinement followed by CTF refinement, polishing, and postprocessing. Final maps were interpreted by applying a lowpass filter of 4 and 4.7 Å, respectively, as Erm still showed less defined density than the ribosome core. The local resolution for the final maps was calculated using RELION's own algorithm (figs. S17 to S19).

Model building and structure analysis

The atomic coordinates of *E. coli* 50*S* precursor (PDB ID: 6GC7) and Erm (PDB ID: 1QAM) was docked in the final cryo-EM maps of state II having two different conformations of ErmC′ using ChimeraX, and N6-mustard–modified A2058 was de novo modeled. The refinement was performed using phenix.real_space_refinement (*65*). The model building was carried out using COOT v.0.9.8.93 (*66*). The model for state III was built in the same manner using the mature 50*S* atomic coordinates (PDB ID: 6GC8). The final model quality was checked using the comprehensive validation module in Phenix (Molprobity). Figures were prepared in ChimeraX, PyMOL (The PyMOL Molecular Graphics System, version 2.4.1), and Adobe Illustrator 2021.

Site-specific labeling of ribosomal precursors

The cryo-EM map of the Erm–ribosomal precursor complex showed that H39 is in proximity of the binding site of Erm. To tag ribosomes at H39, a slight modified protocol of the one reported by Marshall *et al.* (*37*) and Dorywalska *et al.* (*38*) was implemented (fig. S11A). Briefly, H39 was replaced by an artificial hairpin by mutation in 23*S* rRNA introduced by polymerase chain reaction–based overlap—extension protocol in the U2552C containing p278MS2 plasmid. The mutated plasmids were then transformed into DH5α cells containing pCI^{857} plasmids (a gift from R. Green, John Hopkins University, USA) and grown at 42°C until OD_{600} reached ~0.5. The culture was chilled for 40 min to obtain runout ribosomes before cells were harvested at 5180*g* for 15 min (JLA-9.1000 rotor, Beckman and Coulter). Total crude ribosome was purified from the lysate and dialyzed as previously discussed. The dialyzed product was subjected to sucrose gradient ultracentrifugation, and precursor fractions were isolated as previously described.

A total of 100 nM (final concentration) of this concentrated product was mixed with 10× excess of Cy3-tagged oligos having a sequence complementary to the modified H39 sequence in a reaction buffer similar to the methylation buffer composition as mentioned above. The reaction mixture was heated to 42°C for 10 min and gradually cooled to 37°C over the course of 2 hours. The reaction mixture was then added into an Amicon Ultra-4 Centrifugal Filter Unit (100-kDa cutoff), and excess oligos was washed away by passing 10× volumes of reaction buffer. The volume was reduced to 100 μl, and the emission spectra were obtained by exciting at 520 nm to check for the Cy3's characteristic spectrum. Control reactions were also put which contained precursor fractions without H39 mutations and processed in a similar manner. Emission spectra of the control reaction were taken to confirm that the oligos did not attach nonspecifically to ribosomes which do not contain H39-modified hairpins.

The NTD and CTD of Erm42 were labeled individually to probe the differential dynamics of each domain when bound to the ribosome precursor. The NTD contains a single intrinsic cysteine residue (C60) which was used to tag Cy5 maleimide (Amersham Cy5 dye mono-reactive maleimide; code: PA15131) following the manufacturer's protocol. The CTD was tagged by generating C60A/S263C Erm mutant. CD spectroscopy (fig. S11B) (*67*) and scintillation assay (fig. S11C) (*47*) confirmed that the mutant exhibited similar functional and structural characteristics as compared to the native enzyme (wild type).

smFRET data collection and analysis

The interaction between ribosome precursors and Erm was investigated using smFRET. Cy3-labeled ribosome precursors were immobilized on a passivated quartz surface, and Cy5-labeled Erm protein was introduced in the chamber. smFRET imaging was performed using a homebuilt objective type TIRF setup, equipped with dual laser lines (532 and 635 nm) and a scientific Complementary Metal-Oxide–Semiconductor (sCMOS) camera. Emission from donor and acceptor fluorophores was collected through spectral filters, and the E_{FRET} was calculated after correcting for bleed-through and direct excitation of the acceptor. Data analysis, including trace selection, filtering, and E_{FRET} calculations, were performed using ImageJ (*68*), Python 3.11.9 (*69*), and OriginLab 2021 (*70*). The experiments were conducted with Cy5 conjugated to either the CTD or NTD of Erm, and the resulting E_{FRET} histograms along with TDPs were analyzed. Detailed information about surface preparation, data acquisition, and analysis parameters can be found in the Supplementary Materials.

Supplementary Materials

This PDF file includes:

Supplementary Text
Figs. S1 to S19
Tables S1 and S2
References

REFERENCES AND NOTES

1. R. Laxminarayan, The overlooked pandemic of antimicrobial resistance. *Lancet* **399**, 606–607 (2022).
2. M. K. Walker, S. S. Kadri, Antibiotic resistance incidence or proportions: Where does the greatest burden lie? *Lancet Infect. Dis.* **24**, 1291–1293 (2024).
3. C. J. H. von Wintersdorff, J. Penders, J. M. van Niekerk, N. D. Mills, S. Majumder, L. B. van Alphen, P. H. M. Savelkoul, P. F. G. Wolffs, Dissemination of antimicrobial resistance in microbial ecosystems through horizontal gene transfer. *Front. Microbiol.* **7**, 173 (2016).
4. A. J. Schaenzer, G. D. Wright, Antibiotic resistance by enzymatic modification of antibiotic targets. *Trends Mol. Med.* **26**, 768–782 (2020).
5. J. Poehlsgaard, S. Douthwaite, The bacterial ribosome as a target for antibiotics. *Nat. Rev. Microbiol.* **3**, 870–881 (2005).
6. D. N. Wilson, V. Hauryliuk, G. C. Atkinson, A. J. O'Neill, Target protection as a key antibiotic resistance mechanism. *Nat. Rev. Microbiol.* **18**, 637–648 (2020).
7. P. Gupta, S. Sothiselvam, N. Vázquez-Laslop, A. S. Mankin, Deregulation of translation due to post-transcriptional modification of rRNA explains why erm genes are inducible. *Nat. Commun.* **4**, 1984 (2013).
8. T. Tenson, M. Lovmar, M. Ehrenberg, The mechanism of action of macrolides, lincosamides and streptogramin B reveals the nascent peptide exit path in the ribosome. *J. Mol. Biol.* **330**, 1005–1014 (2003).
9. G. P. Dinos, The macrolide antibiotic renaissance. *Br. J. Pharmacol.* **174**, 2967–2983 (2017).
10. B. Weisblum, Erythromycin resistance by ribosome modification. *Antimicrob. Agents Chemother.* **39**, 577–585 (1995).
11. M. M. Almutairi, S. R. Park, S. Rose, D. A. Hansen, N. Vázquez-Laslop, S. Douthwaite, D. H. Sherman, A. S. Mankin, Resistance to ketolide antibiotics by coordinated expression of rRNA methyltransferases in a bacterial producer of natural ketolides. *Proc. Natl. Acad. Sci. U.S.A.* **112**, 12956–12961 (2015).
12. M. S. Svetlov, E. A. Syroegin, E. V. Aleksandrova, G. C. Atkinson, S. T. Gregory, A. S. Mankin, Y. S. Polikanov, Structure of Erm-modified 70S ribosome reveals the mechanism of macrolide resistance. *Nat. Chem. Biol.* **17**, 412–420 (2021).
13. P. V. Sergiev, N. A. Aleksashin, A. A. Chugunova, Y. S. Polikanov, O. A. Dontsova, Structural and evolutionary insights into ribosomal RNA methylation. *Nat. Chem. Biol.* **14**, 226–235 (2018).
14. R. Bhujbalrao, R. Anand, Deciphering determinants in ribosomal methyltransferases that confer antimicrobial resistance. *J. Am. Chem. Soc.* **141**, 1425–1429 (2019).
15. P. Z. Kozbial, A. R. Mushegian, Natural history of S-adenosylmethionine-binding proteins. *BMC Struct. Biol.* **5**, 19 (2005).
16. N. Pulicherla, L. A. Pogorzala, Z. Xu, F. N. Musayev, J. N. Scarsdale, E. A. Sia, G. M. Culver, J. P. Rife, Structural and functional divergence within the Dim1/KsgA family of rRNA methyltransferases. *J. Mol. Biol.* **391**, 884–893 (2009).
17. K. E. Guja, K. Venkataraman, E. Yakubovskaya, H. Shi, E. Mejia, E. Hambardjieva, A. W. Karzai, M. Garcia-Diaz, Structural basis for S-adenosylmethionine binding and methyltransferase activity by mitochondrial transcription factor B1. *Nucleic Acids Res.* **41**, 7947–7959 (2013).
18. K. Goedecke, M. Pignot, R. S. Goody, A. J. Scheidig, E. Weinhold, Structure of the N6-adenine DNA methyltransferase M•TaqI in complex with DNA and a cofactor analog. *Nat. Struct. Biol.* **8**, 121–125 (2001).
19. J. R. Horton, X. Zhang, R. M. Blumenthal, X. Cheng, Structures of *Escherichia coli* DNA adenine methyltransferase (Dam) in complex with a non-GATC sequence: Potential implications for methylation-independent transcriptional repression. *Nucleic Acids Res.* **43**, 4296–4308 (2015).
20. E. Abdelraheem, B. Thair, R. F. Varela, E. Jockmann, D. Popadić, H. C. Hailes, J. M. Ward, A. M. Iribarren, E. S. Lewkowicz, J. N. Andexer, P. L. Hagedoorn, U. Hanefeld, Methyltransferases: Functions and applications. *ChemBioChem* **23**, e202200212 (2022).
21. I. Pokkunuri, W. S. Champney, Characteristics of a 50S ribosomal subunit precursor particle as a substrate for ermE methyltransferase activity and erythromycin binding in *Staphylococcus aureus*. *RNA Biol.* **4**, 147–153 (2007).
22. J. H. Davis, J. R. Williamson, Structure and dynamics of bacterial ribosome biogenesis. *Philos. Trans. R. Soc. B Biol. Sci.* **372**, 20160181 (2017).

23. T. Arai, K. Ishiguro, S. Kimura, Y. Sakaguchi, T. Suzuki, T. Suzuki, Single methylation of 23S rRNA triggers late steps of 50S ribosomal subunit assembly. *Proc. Natl. Acad. Sci. U.S.A.* **112**, E4707–E4716 (2015).
24. S. Ward, A. Childs, C. Staley, C. Waugh, J. A. Watts, A. M. Kotowska, R. Bhosale, A. N. Borkar, Integrating cryo-OrbiSIMS with computational modelling and metadynamics simulations enhances RNA structure prediction at atomic resolution. *Nat. Commun.* **15**, 4367 (2024).
25. M. K. Passarelli, A. Pirkl, R. Moellers, D. Grinfeld, F. Kollmer, R. Havelund, C. F. Newman, P. S. Marshall, H. Arlinghaus, M. R. Alexander, A. West, S. Horning, E. Niehuis, A. Makarov, C. T. Dollery, I. S. Gilmore, The 3D OrbiSIMS—Label-free metabolic imaging with subcellular lateral resolution and high mass-resolving power. *Nat. Methods* **14**, 1175–1183 (2017).
26. V. Mai, L. R. Comstock, Synthesis of an azide-bearing N-mustard analogue of S-adenosyl-L-methionine. *J. Org. Chem.* **76**, 10319–10324 (2011).
27. M. Ramadan, N. K. Bremner-Hay, S. A. Carlson, L. R. Comstock, Synthesis and evaluation of *N*6-substituted azide- and alkyne-bearing *N*-mustard analogs of *S*-adenosyl-l-methionine. *Tetrahedron* **70**, 5291–5297 (2014).
28. K. Sheng, N. Li, J. N. Rabuck-Gibbons, X. Dong, D. Lyumkis, J. R. Williamson, Assembly landscape for the bacterial large ribosomal subunit. *Nat. Commun.* **14**, 5220 (2023).
29. B. Qin, S. M. Lauer, A. Balke, C. H. Vieira-Vieira, J. Bürger, T. Mielke, M. Selbach, P. Scheerer, C. M. T. Spahn, R. Nikolay, Cryo-EM captures early ribosome assembly in action. *Nat. Commun.* **14**, 898 (2023).
30. X. Ni, J. H. Davis, N. Jain, A. Razi, S. Benlekbir, A. G. McArthur, J. L. Rubinstein, R. A. Britton, J. R. Williamson, J. Ortega, YphC and YsxC GTPases assist the maturation of the central protuberance, GTPase associated region and functional core of the 50S ribosomal subunit. *Nucleic Acids Res.* **44**, 8442–8455 (2016).
31. R. Nikolay, T. Hilal, B. Qin, T. Mielke, J. Bürger, J. Loerke, K. Textoris-Taube, K. H. Nierhaus, C. M. T. Spahn, Structural visualization of the formation and activation of the 50S ribosomal subunit during in vitro reconstitution. *Mol. Cell* **70**, 881–893.e3 (2018).
32. W. Wang, W. Li, X. Ge, K. Yan, C. S. Mandava, S. Sanyal, N. Gao, Loss of a single methylation in 23S rRNA delays 50S assembly at multiple late stages and impairs translation initiation and elongation. *Proc. Natl. Acad. Sci. U.S.A.* **117**, 15609–15619 (2020).
33. D. S. D. Larsson, S. Kanchugal P, M. Selmer, Structural consequences of deproteinating the 50S ribosome. *Biomolecules* **12**, 1605 (2022).
34. R. Röhl, K. H. Nierhaus, Assembly map of the large subunit (50S) of *Escherichia coli* ribosomes. *Proc. Natl. Acad. Sci. U.S.A.* **79**, 729–733 (1982).
35. R. Bhujbalrao, K. Gavvala, R. K. Singh, J. Singh, C. Boudier, S. Chakrabarti, G. N. Patwari, Y. Mély, R. Anand, Identification of allosteric hotspots regulating the ribosomal RNA binding by antibiotic resistance-conferring Erm methyltransferases. *J. Biol. Chem.* **298**, 102208 (2022).
36. G. Schluckebier, P. Zhong, K. D. Stewart, T. J. Kavanaugh, C. Abad-Zapatero, The 2.2 Å structure of the rRNA methyltransferase ErmC′ and its complexes with cofactor and cofactor analogs: Implications for the reaction mechanism. *J. Mol. Biol.* **289**, 277–291 (1999).
37. R. A. Marshall, M. Dorywalska, J. D. Puglisi, Irreversible chemical steps control intersubunit dynamics during translation. *Proc. Natl. Acad. Sci. U.S.A.* **105**, 15364–15369 (2008).
38. M. Dorywalska, S. C. Blanchard, R. L. Gonzalez, H. D. Kim, S. Chu, J. D. Puglisi, Site-specific labeling of the ribosome for single-molecule spectroscopy. *Nucleic Acids Res.* **33**, 182–189 (2005).
39. M. Brinkley, A brief survey of methods for preparing protein conjugates with dyes, haptens and crosslinking reagents. *Bioconjug. Chem.* **3**, 2–13 (1992).
40. L. D. Moore, T. Le, G. Fan, DNA methylation and its basic function. *Neuropsychopharmacology* **38**, 23–38 (2013).
41. H. Hori, Methylated nucleosides in tRNA and tRNA methyltransferases. *Front. Genet.* **5**, 144 (2014).
42. X. Yang, Y. Yang, B.-F. Sun, Y.-S. Chen, J.-W. Xu, W.-Y. Lai, A. Li, X. Wang, D. P. Bhattarai, W. Xiao, H.-Y. Sun, Q. Zhu, H.-L. Ma, S. Adhikari, M. Sun, Y.-J. Hao, B. Zhang, C.-M. Huang, N. Huang, G.-B. Jiang, Y.-L. Zhao, H.-L. Wang, Y.-P. Sun, Y.-G. Yang, 5-methylcytosine promotes mRNA export—NSUN2 as the methyltransferase and ALYREF as an m5C reader. *Cell Res.* **27**, 606–625 (2017).
43. Z. T. Laughlin, S. Nandi, D. Dey, N. Zelinskaya, M. A. Witek, P. Srinivas, H. A. Nguyen, E. G. Kuiper, L. R. Comstock, C. M. Dunham, G. L. Conn, 50S subunit recognition and modification by the *Mycobacterium tuberculosis* ribosomal RNA methyltransferase TlyA. *Proc. Natl. Acad. Sci. U.S.A.* **119**, e2120352119 (2022).
44. P. Srinivas, M. Nosrati, N. Zelinskaya, D. Dey, L. R. Comstock, C. M. Dunham, G. L. Conn, 30S subunit recognition and G1405 modification by the aminoglycoside-resistance 16S ribosomal RNA methyltransferase RmtC. *Proc. Natl. Acad. Sci. U.S.A.* **120**, e2304128120 (2023).
45. W. Ren, J. Lu, M. Huang, L. Gao, D. Li, G. G. Wang, J. Song, Structure and regulation of ZCCHC4 in m6A-methylation of 28S rRNA. *Nat. Commun.* **10**, 5042 (2019).
46. M. Fislage, M. Roovers, I. Tuszynska, J. M. Bujnicki, L. Droogmans, W. Versées, Crystal structures of the tRNA: m 2 G6 methyltransferase Trm14/TrmN from two domains of life. *Nucleic Acids Res.* **40**, 5149–5161 (2012).
47. J. Singh, R. Raina, K. R. Vinothkumar, R. Anand, Decoding the mechanism of specific RNA targeting by ribosomal methyltransferases. *ACS Chem. Biol.* **17**, 829–839 (2022).
48. J. A. Dunkle, K. Vinal, P. M. Desai, N. Zelinskaya, M. Savic, D. M. West, G. L. Conn, C. M. Dunham, Molecular recognition and modification of the 30S ribosome by the aminoglycoside-resistance methyltransferase NpmA. *Proc. Natl. Acad. Sci. U.S.A.* **111**, 6275–6280 (2014).
49. G. Maravić, J. M. Bujnicki, M. Feder, S. Pongor, M. Flögel, Alanine-scanning mutagenesis of the predicted rRNA-binding domain of ErmC′ redefines the substrate-binding site and suggests a model for protein–RNA interactions. *Nucleic Acids Res.* **31**, 4941–4949 (2003).
50. C. T. Madsen, L. Jakobsen, K. Buriánková, F. Doucet-Populaire, J.-L. Pernodet, S. Douthwaite, Methyltransferase Erm (37) slips on rRNA to confer atypical resistance in *Mycobacterium tuberculosis*. *J. Biol. Chem.* **280**, 38942–38947 (2005).
51. N. C. Stephan, A. B. Ries, D. Boehringer, N. Ban, Structural basis of successive adenosine modifications by the conserved ribosomal methyltransferase KsgA. *Nucleic Acids Res.* **49**, 6389–6398 (2021).
52. J. Zou, W. Zhang, H. Zhang, X. D. Zhang, B. Peng, J. Zheng, Studies on aminoglycoside susceptibility identify a novel function of KsgA to secure translational fidelity during antibiotic stress. *Antimicrob. Agents Chemother.* **62**, e00853-18 (2018).
53. H. J. Lee, S. T. Jhang, H. J. Jin, Potential target site for inhibitors in MLSB antibiotic resistance. *Antibiotics* **10**, 264 (2021).
54. I. P. Foik, I. Tuszynska, M. Feder, E. Purta, F. Stefaniak, J. M. Bujnicki, Novel inhibitors of the rRNA ErmC′ methyltransferase to block resistance to macrolides, lincosamides, streptogramine B antibiotics. *Eur. J. Med. Chem.* **146**, 60–67 (2018).
55. J. Clancy, B. J. Schmieder, J. W. Petitpas, M. Manousos, J. A. Williams, J. A. Faiella, A. E. Girard, P. R. McGuirk, Assays to detect and characterize synthetic agents that inhibit the ErmC methyltransferase. *J. Antibiot.* **48**, 1273–1279 (1995).
56. M. Feder, E. Purta, L. Koscinski, S. Čubrilo, G. Maravic Vlahovicek, J. M. Bujnicki, Virtual screening and experimental verification to identify potential inhibitors of the ErmC methyltransferase responsible for bacterial resistance against macrolide antibiotics. *ChemMedChem* **3**, 316–322 (2008).
57. B. C. Goh, X. Xiang, J. Lescar, P. C. Dedon, Crystal structure and functional analysis of mycobacterial erythromycin resistance methyltransferase Erm38 reveals its RNA-binding site. *J. Biol. Chem.* **298**, 101571 (2022).
58. L. Yu, A. M. Petros, A. Schnuchel, P. Zhong, J. M. Severin, K. Walter, T. F. Holzman, S. W. Fesik, Solution structure of an rRNA methyltransferase (ErmAM) that confers macrolide-lincosamide-streptogramin antibiotic resistance. *Nat. Struct. Biol.* **4**, 483–489 (1997).
59. A. Stsiapanava, M. Selmer, Crystal structure of ErmE-23S rRNA methyltransferase in macrolide resistance. *Sci. Rep.* **9**, 14607 (2019).
60. E. M. Youngman, R. Green, Affinity purification of in vivo-assembled ribosomes for in vitro biochemical analysis. *Methods* **36**, 305–312 (2005).
61. Q. Sun, A. Vila-Sanjurjo, M. O'Connor, Mutations in the intersubunit bridge regions of 16S rRNA affect decoding and subunit–subunit interactions on the 70S ribosome. *Nucleic Acids Res.* **39**, 3321–3330 (2011).
62. B. Desmolaize, S. Rose, R. Warrass, S. Douthwaite, A novel Erm monomethyltransferase in antibiotic-resistant isolates of *Mannheimia haemolytica* and *Pasteurella multocida*. *Mol. Microbiol.* **80**, 184–194 (2011).
63. G. Zhang, S. L. Richardson, Y. Mao, R. Huang, Design, synthesis, and kinetic analysis of potent protein N-terminal methyltransferase 1 inhibitors. *Org. Biomol. Chem.* **13**, 4149–4154 (2015).
64. E. F. Pettersen, T. D. Goddard, C. C. Huang, E. C. Meng, G. S. Couch, T. I. Croll, J. H. Morris, T. E. Ferrin, UCSF ChimeraX: Structure visualization for researchers, educators, and developers. *Protein Sci.* **30**, 70–82 (2021).
65. P. D. Adams, P. V. Afonine, G. Bunkóczi, V. B. Chen, I. W. Davis, N. Echols, J. J. Headd, L.-W. Hung, G. J. Kapral, R. W. Grosse-Kunstleve, A. J. McCoy, N. W. Moriarty, R. Oeffner, R. J. Read, D. C. Richardson, J. S. Richardson, T. C. Terwilliger, P. H. Zwart, PHENIX: A comprehensive Python-based system for macromolecular structure solution. *Acta Crystallogr. D Biol. Crystallogr.* **65**, 1074 (2009).
66. P. Emsley, K. Cowtan, Coot: Model-building tools for molecular graphics. *Biol. Crystallogr.* **60**, 2126–2132 (2004).
67. S. M. Kelly, N. C. Price, The use of circular dichroism in the investigation of protein structure and function. *Curr. protein Pept. Sci.* **1**, 349–384 (2000).
68. C. A. Schneider, W. S. Rasband, K. W. Eliceiri, NIH Image to ImageJ: 25 years of image analysis. *Nat. Methods* **9**, 671–675 (2012).
69. W. McKinney, *Python for Data Analysis* (O'Reilly Media Inc., 2022).
70. *V. OriginPro* (OriginLab Corporation, 2016).
71. M. Levitus, S. Ranjit, Cyanine dyes in biophysical research: The photophysics of polymethine fluorescent dyes in biomolecular environments. *Q. Rev. Biophys.* **44**, 123–151 (2011).
72. A. D. Edelstein, M. A. Tsuchida, N. Amodaj, H. Pinkard, R. D. Vale, N. Stuurman, Advanced methods of microscope control using μManager software. *J. Biol. methods* **1**, e10 (2014).
73. A. K. Pati, Z. Kilic, M. I. Martin, D. S. Terry, A. Borgia, S. Bar, S. Jockusch, R. Kiselev, R. B. Altman, S. C. Blanchard, Recovering true FRET efficiencies from smFRET investigations requires triplet state mitigation. *Nat. Methods* **21**, 1222–1230 (2024).

74. J. Malicka, I. Gryczynski, J. Fang, J. Kusba, J. R. Lakowicz, Photostability of Cy3 and Cy5-labeled DNA in the presence of metallic silver particles. *J. Fluoresc.* **12**, 439–447 (2002).
75. F. Yuan, L. Griffin, L. Phelps, V. Buschmann, K. Weston, N. L. Greenbaum, Use of a novel Förster resonance energy transfer method to identify locations of site-bound metal ions in the U2-U6 snRNA complex. *Nucleic Acids Res.* **35**, 2833–2845 (2007).
76. K. Okamoto, Analyzing single molecule FRET trajectories using HMM. *Methods Mol. Biol.* **1552**, 103–113 (2017).
77. P. V. Cornish, D. N. Ermolenko, H. F. Noller, T. Ha, Spontaneous intersubunit rotation in single ribosomes. *Mol. Cell* **30**, 578–588 (2008).
78. M. Blanco, N. G. Walter, "Chapter 9 - Analysis of complex single-molecule FRET time trajectories" in *Single Molecule Tools: Fluorescence Based Approaches, Part A, N. G. B. T.-M.*, E. Walter, Ed. (Academic Press, 2010; https://sciencedirect.com/science/article/pii/S0076687910720115), vol. 472, pp. 153–178.

Acknowledgments: R.A. acknowledges support from the Industrial Research and Consultancy Centre (IRCC), IIT Bombay. A.C. acknowledges support from the Industrial Research and Consultancy Centre (IRCC) and SCAN, IIT Bombay. C.E. and M.P. would like to thank all past and present members of the Structural Biochemistry group at the University of Regensburg. A.N.B. acknowledges the Anne McLaren Fellowship granted by the University of Nottingham. S.S. and R.M. acknowledge the PMRF and IIT Bombay for fellowship. S.B. acknowledges IIT Bombay for fellowship. A.D.A. acknowledges UGC for fellowship. S.S., R.M., A.C., and R.A. would like to thank Suman De (University of Sheffield, UK) and P. P. Mishra (Saha Institute of Nuclear Physics, India) for technical help regarding smFRET data collection. We also thank the ANRF and IoE-supported national cryo-EM facility at IIT Bombay. We also wish to thank the cryo-EM facilities at IIT Delhi and the University of Regensburg for initial data collection and screening.

Funding: This work was funded by the DBT Wellcome Trust India Alliance grant IA/S/19/1/504293 (to R.A.), SERB grant IPA/2020/000413 (to R.A.), SERB grant CRG/2022/002656 (to P.S.K.), SERB grant CRG/2021/001992 (to P.I.P.), DBT grant number BT/INF/22/SP23026/2017 (to A.C.), Emmy Noether Programme DFG, EN 1204/1-1 project number 394580547 (to CE), and EPSRC grant EP/P029868/1 (to A.N.B.) which funded the cryogenic OrbiSIMS instrument at University of Nottingham, UK. **Author contributions:** Conceptualization: R.A. Methodology: S.S., R.M., M.P., S.B., A.N.B., P.I.P., C.E., A.C., P.S.K., and R.A. Software: R.M. and A.N.B. Validation: S.S., R.M., M.P., A.N.B., P.I.P., P.S.K., and R.A. Formal analysis: S.S., R.M., S.B., A.D.A., A.N.B., P.I.P., P.S.K., and R.A. Investigation: S.S., R.M., M.P., S.B., A.N.B., P.I.P., and R.A. Resources: P.I.P., C.E., A.C., and R.A. Data curation: S.S., R.M., M.P., S.B., A.D.A., A.N.B., P.I.P., A.C., P.S.K., and R.A. Writing—original draft: S.S., R.M., and R.A. Writing—review and editing: S.S., R.M., M.P., A.D.A., A.N.B., P.I.P., C.E., A.C., P.S.K., and R.A. Visualization: S.S., R.M., A.D.A., A.N.B., P.I.P., A.C., and R.A. Supervision: A.N.B., P.I.P., C.E., A.C., and R.A. Project administration: R.A. Funding acquisition: A.N.B., P.I.P., C.E., A.C., P.S.K., and R.A. **Competing interests:** The authors declare that they have no competing interests. **Data and materials availability:** The cryo-EM map and model for the state I, state II (C-I), state II (C-II), and state III have been deposited into EM Data Bank and PDB under accession codes EMD-61613; EMD-61625, PDB-9JNS; EMD-61781, PDB-9JSR; and EMD-61605, PDB-9JMK, respectively. Other atomic coordinates used in this study are available from the PDB under the following accession codes: 1QAM for Erm, 6GC7 for a ribosomal precursor, and 6GC8 for a mature 50*S* subunit. The cryo-OrbiSIMS data have been deposited into the Nottingham Research Repository and can be accessed through the DOI: 10.17639/nott.7481.

Submitted 1 July 2025
Accepted 27 October 2025
Published 26 November 2025
10.1126/sciadv.aea1545